

Determining the nature of IC 10 X-2: A comprehensive study of the OIR emission from an extragalactic BeHMXB

JWAHER ALNAQBI,¹ JOSEPH D. GELFAND,^{1,2} PAYASWINI SAIKIA,¹ CRAIG HEINKE,³ M. C. BAGLIO,⁴ DAVID M. RUSSELL,¹
GUOBAO ZHANG,⁵ ANTONIOS MANOUSAKIS,⁶ IVAN YU. KATKOV,^{1,7} AND FRASER LEWIS^{8,9}

¹Center for Astrophysics and Space Science (CASS), New York University Abu Dhabi, PO Box 129188, Abu Dhabi, UAE

²Affiliate Member, Center for Cosmology and Particle Physics (CCPP), New York University, 726 Broadway, New York, NY 10003

³Physics Dept., CCIS 4-183, University of Alberta, Edmonton, AB T6G 2E1, Canada

⁴INAF, Osservatorio Astronomico di Brera, Via Bianchi 46, Merate (LC), I-23807, Italy

⁵Yunnan Observatories Chinese Academy of Sciences

⁶Department of Applied Physics and Astronomy, College of Sciences, University of Sharjah POBox 27272 University City, Sharjah, UAE
and Sharjah Academy for Astronomy, Space Sciences and Technology (SAASST), POBox 27272 University City, Sharjah, UAE

⁷Sternberg Astronomical Institute, Lomonosov Moscow State University, Universitetskij pr., 13, Moscow, 119234, Russia

⁸Faulkes Telescope Project, School of Physics and Astronomy, Cardiff University, The Parade, Cardiff, CF24 3AA Wales, UK

⁹Astrophysics Research Institute, Liverpool John Moores University, 146 Brownlow Hill, Liverpool L3 5RF, UK

(Revised January 14, 2025)

Submitted to ApJ

ABSTRACT

We present a comprehensive analysis of the optical and infrared (IR) properties of high-mass X-ray binary (HMXB) IC 10 X-2, classified as a super-giant HMXB and super-fast X-ray transient (SFXT) by previous work. Our analysis of regular (daily and weekly) observations by both the Zwicky Transient Factory and Las Cumbres Observatory over a 5 year period indicates both periodic flares and variations in the apparent magnitude and color with a ~ 26.5 d period – likely the orbital period of this binary system. The periodic flaring suggests the stellar companion is a Be star, with flares resulting from increased accretion onto the neutron star when it enters the stellar decretion disk. The periodic variations in the optical/IR brightness and color likely result from orbital variations in the Hydrogen column density along the line of sight or a transient accretion disk around the neutron star. Lastly, the numerous, short duration, episodes where IC 10 X-2 is significantly “redder” or “bluer” than normal likely result from clumps within this system – which can accrete onto the neutron star (causing IC 10 X-2 to appear bluer), or pass through the line of sight (causing IC 10 X-2 to appear redder). These results substantially increase our understanding of the evolution of this source, a significant source of ionizing photons in its host galaxy IC 10, a low mass, metal-poor starburst galaxy similar in many respect to those thought to be common in the early Universe.

Keywords: X-rays: binaries; stars: emission-line, Be; supergiants; dust, extinction; X-rays: individual: IC 10 X-2

1. INTRODUCTION

High-mass X-ray binaries (HMXBs) are believed to be systems where a compact object, i.e., a neutron star (NS) or a black hole (BH), are gravitationally bound to a more massive star, typically an O- or B-type companion, either on the main sequence phase or in a later super-

giant (SG) evolutionary stage. HMXBs are primarily classified by the mode of accretion from the stellar companion onto the compact object, which in turn depends on the nature of the companion.

There are two primary modes of accretion, and hence primary classes (e.g., [Tan 2021](#)) of HMXBs, the first of which is Bondi (or “wind-fed,” in the case of HMXBs; [Shakura et al. 2015](#)) accretion of material ejected by a, typically SG, star (sgHMXB). SG systems often

Corresponding author: U

have relatively short orbital periods ($\lesssim 20$ days; e.g., [Townsend et al. 2011](#)) and, during quiescence, the dominant source of the optical emission is the SG star due to its high luminosity. In these systems, absorbing clumps are frequently detected in optical observations as decreases in brightness, with larger amplitude decreases observed at shorter wavelengths. Flares originate from clumps accreting onto the compact object, and are observed primarily at infrared (IR), optical, ultraviolet (UV), and X-ray wavebands.

In the second class, the stellar companion typically an Oe/Be star, and hence systems of this type are referred to as BeHMXBs. In these systems, the compact object (generally a NS, [Shi et al. 2015](#)) primarily accretes material from the decretion disk created by the highly asymmetric wind of the companion star, infrequently supplemented by minor Roche lobe overflow from the star onto the compact object (e.g., [Chaty 2018](#)). The orbital passage of the NS through the circumstellar disk results in periodic outbursts or flares with X-ray luminosities up to $\sim 10^{38}$ erg/s that can last for days or weeks ([Ducci et al. 2022](#)) in this and other (IR, optical, and UV) wavebands (e.g., [Alcock et al. 2001](#); [Bird 2012](#)).

Be systems can be identified through these periodic flares or outbursts, that are frequently used to determine the orbital period in these systems (e.g., [Alcock et al. 2001](#); [Jain et al. 2009](#)). Be systems can also be distinguished by high extinction or reddening caused by the material in the disk, and strong H α emission, in addition to appearing redder when fainter (e.g., [Alcock et al. 2001](#)). While the optical emission from Be systems is generally dominated by the companion star, accretion onto the compact object can also significantly contribute during periodic flares or outbursts.

Some Be and sgHMXBs are observed to be Supergiant Fast X-ray Transients (SFXTs), i.e. system that exhibit short-duration, intense X-ray flares detected at any orbital phase – attributed to the accretion of relatively distant clumps formed in the stellar wind of the companion star onto the compact object ([Ducci et al. 2009](#); [Oskinova et al. 2007](#); [Walter et al. 2007](#); [Bandyopadhyay et al. 2008](#)). They can also exhibit short (\sim a few hours long) periods of significant X-ray (and optical) variability ([Pellizza et al. 2006](#)) as a result of clumps wandering through the line of sight and blocking some of the emission, leading dips in its light curves ([Drave et al. 2013](#); [Rampy et al. 2009](#); [Bozzo et al. 2017](#)). About half of SFXTs show X-ray pulsations ([Sidoli 2013](#)), proving that many (if not most) contain neutron stars. It is believed that some SFXTs are descendants of BeHMXBs ([Liu et al. 2011](#)). For instance, systems that were clas-

sified as SFXTs in X-ray showed periodic flares in their X-ray folded light curves ([Jain et al. 2009](#)), and strong H α emission in optical as in Be systems (see Figure 1 in [Hare et al. 2019](#) and Figure 10 in [Coe et al. 2021](#)). However, other SFXTs were noticed to house SG stars and accrete via Bondi accretion ([Shakura et al. 2014](#)).

The optical and IR emission of HMXBs provides important insight into the nature of the stellar companion, as well as the warm gas in these systems which likely comprise the bulk of the material ejected by the star. However, given the high N_{H} observed towards most Galactic HMXBs, emission in these wavebands is often hard to detect for such sources. Therefore, studying extragalactic HMXBs is important for understanding the origin of the optical and IR emission of such objects. IC 10 X–2 is a HMXB first identified due to a massive X-ray outburst ($\sim 100\times$ increase in flux) it produced 2003, during which it was the second X-ray brightest object in the IC 10 galaxy ([Wang et al. 2005](#); [Kwan et al. 2018](#)). [Laycock et al. \(2014\)](#) used the Chandra position (RA: 00:20:20.94, Dec: 59:17:59.0) to find the optical counterpart, analyzed the X-ray and optical spectra of IC 10 X–2, and concluded that the companion in the system is a blue SG. The optical spectrum showed a smooth continuum and revealed strong H α emission and a complex of FeII permitted and forbidden emission lines, similar to B[e] stars, i.e., B-type stars with forbidden emission lines. The HeI emission and forbidden lines IC 10 X–2 studied by [Laycock et al. \(2014\)](#) have also been detected in some sgB[e] systems ([Lamers et al. 1998](#)).

The hard X-ray spectrum of IC 10 X–2 suggests that the compact object is a NS. A more recent study by [Kwan et al. \(2018\)](#) of the optical and IR light curve and spectrum of IC 10 X–2 revealed that the properties of the HeI, Paschen- γ , and Paschen- β emission lines, and the mid-IR colors and magnitudes, showed strong similarities to those in Luminous Blue Variables (LBV) or LBV candidates (LBVc), and hence suggested the companion of IC 10 X–2 is an LBV/LBVc.

In Section 2, we present the Zwicky Transient Facility (ZTF) and Las Cumbres Observatory (LCO) data analyzed in this work. We present in Section 3 the light curves and color-magnitude diagrams of this object, which we use to identify flares (§3.3) and periodic variations in both the brightness and color of this source (§3.4). In Section 4, we discuss the physical implications of our findings, and summarize our results in §5).

2. OBSERVATIONAL DATA

In this section, we describe the data analyzed in this work, obtained from ZTF (Section 2.1), and the global telescope network of Las Cumbres Observatory (LCO;

Table 1. Description of the ZTF, LCO, Gaia DR3 filters.

	ZTF ^a		LCO ^b			Gaia DR3 ^c		
Cadence	~ 1 day		~ 1 week					
Filter	z_g	z_r	g'	r'	i'	bp	g	rp
λ_{central} (Å)	4722	6340	4770	6215	7545	5341.29	6605.35	7849.14
FWHM (Å)	1282	1515	1500	1390	1290	2530.79	4365.35	3082.81
MJD range (day)	58252–59264	58254–59264	58084–59262					
Number of data points	323	483	76	79	74			

^a Lau et al. (2021)

^b <https://lco.global/observatory/>

^c <https://gea.esac.esa.int/archive/>

Section 2.2). A summary of the data sets used in this work is provided in Table 1.

2.1. Zwicky Transient Facility

ZTF is an optical time-domain astronomical survey that uses an enhanced CCD camera attached to the Samuel Oschin Telescope at the Palomar Observatory in California, United States (Bellm et al. 2019). It uses three filters (z_g , z_r , and z_i) with improved sensitivity compared to that in Sloan Digital Sky Survey (SDSS), and has the ability to request observations a few hours apart using these filters. The telescope scans the entire Northern sky at night with a cadence of two days. Each data release reports selected automatically detected targets’ light curves; the MJD of a detection, the corresponding magnitude and error, and the target’s position in the sky. We acquired three filters’ data, z_g , z_r , and z_i , of IC 10 X–2 from the Public Data Release 6 (ZTF 2022), retrieved through NASA/IPAC Infrared Science Archive (IRSA) (NASA 2021, retrieved on 23 October 2021). Each filter data set is labeled with an identification number (OID) as listed in Table 2. The angular distance search was less than $1''$ from the target’s right ascension and declination. The z_i filter was not included in further analyses, as there were only 2 detections within our selected time frame (see Table 1).

2.2. LCO

Observations of the source in three SDSS filters (g' , r' and i') were taken ~ 10 minutes apart between 2017 November 27 (MJD 58084) and 2021 July 31 (MJD 59426), using 5-minute exposures with the 1.0-meter telescope, and the 2.0-meter Faulkes Telescope North equipped with the Muscat3 camera, of the Las Cumbres Observatory (LCO) (Brown et al. 2013). The 2.0-meter telescope allows for simultaneous observations in g' , r' , i' , and z' . The data were extracted and calibrated by the X-ray Binary New Early Warning System (XB-NEWS) real-time data analysis pipeline (Russell et al. 2019; Goodwin et al. 2020). XB-NEWS measured IC

10 X-2 coordinates as RA:00:20:20.89 Dec:+59:17:59.2 with accuracy $\lesssim 0.1''$. The statistical error associated with all LCO magnitudes in this work is < 0.09 mag.

We show in Figure 1 images of the IC 10 X-2 field using LCO g' , r' , i' , and a Hubble Space Telescope Advanced Camera for Surveys/Wide Field Channel (HST ACS/WFC) higher resolution image in the $F606W$ filter. We found two bright sources within $2''$ of IC 10 X–2’s coordinates ($\sim 1.6''$ away) in the HST image. This suggests that extraction of LCO photometry with a $2''$ radius at IC 10 X–2’s coordinates should include a brightness contribution from the nearby source. We searched in Gaia DR 3 (Gaia Collaboration et al. 2023) for the magnitude of both sources (IC 10 X-2 and the nearby source) to quantify the nearby source’s contribution to the measured magnitude. The Gaia- g magnitudes were reported in Gaia DR 3 as 19.00 mag for IC 10 X–2 and 20.54 mag for the nearby source, respectively, i.e., one-fourth of IC 10 X–2’s flux. The average magnitude and color measured for the brighter Gaia source is consistent with the average magnitude and color measured in our LCO observations. Therefore, we conclude that the brighter of the two Gaia sources dominate the total emission measured in the observations we analyze which we associate with IC 10 X-2.

3. DATA ANALYSIS AND RESULTS

In this Section, we first discuss the observed IC 10 X–2 multi-band light curve in Section 3.1 and color in Section 3.2, then we identify flares in Section 3.3, and lastly, we search for periodicity in the light curves in Section 3.4.

3.1. Multi-Band Light Curve

Figure 2 shows the apparent i' , r' / z_r , and g' / z_g magnitudes of IC 10 X–2 as measured on different epochs in the observations described in §2. In all five filters, there were epochs when the source was brighter (lower apparent magnitude) than average, with the observed variations ($\sim 1 - 1.5$ magnitudes in the z_g / g' ,

Table 2. Properties of ZTF data on IC 10 X-2 obtained between 2018 May 14 (MJD 58254) and 2019 October 15 (MJD 58771). OID refers to the identification number in the ZTF DR 6 catalog.

OID	Filter	Number of observations	RA (deg)	Dec (deg)
806103100029923	z_g	278	5.086978	59.29979
1809111300028700	z_g	45	5.086909	59.29979
806203100063307	z_r	827	5.087091	59.29981
1809211300074740	z_r	84	5.087093	59.29979
806303100062288	z_i	2	5.087076	59.29979

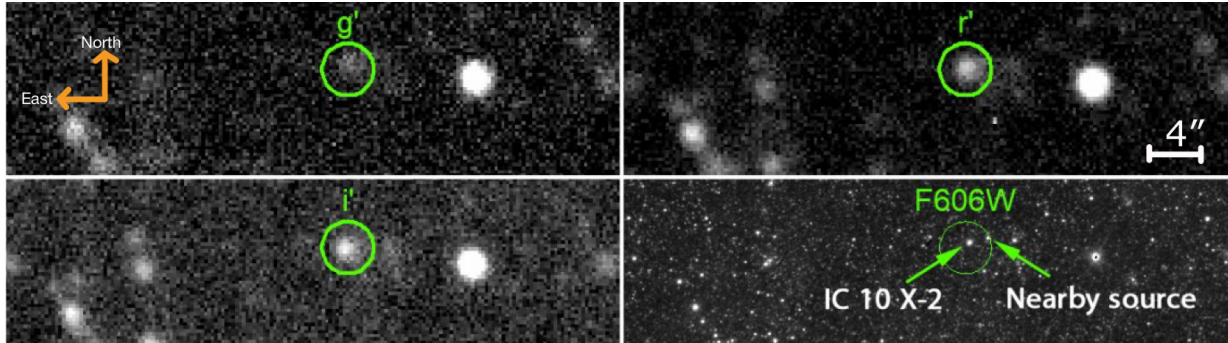


Figure 1. LCO images taken on MJD 59767 (2021 July 7), centered at IC 10 X-2’s coordinates in g' , r' , i' , and HST ACS/WFC $F606W$ filters. The $F606W$ image clearly shows IC 10 X-2 (brightest, on the left) and the nearby source (second brightest, on the right). The region radius in all images is $2''$ and the filter used is indicated on each image.

Table 3. Gaia DR3 details of sources within $2''$ of IC 10 X-2 coordinates.

Gaia ID	RA	Dec	Gaia g (mag)	Gaia $bp - rp$ (mag)
428242947042534784	5.086406836	59.29988915	20.54	NA
428242947052289664	5.087189803	59.29978945	19.00	1.67

z_r / r' filters, and ~ 1 in i') much larger than the typical errors in these measurements (~ 0.08 for z_g / z_r , ~ 0.02 for g' / r' , and ~ 0.05 for i') – suggesting these changes are intrinsic to the source.

3.2. Observed Color

Figure 3 shows the apparent color ($z_g - z_r$, $g' - r'$) as a function of the apparent magnitude (z_g and g' , respectively) measured on a particular epoch. As shown in this Figure, it appears that when IC 10 X-2 is brighter (lower absolute magnitude), its emission is also bluer (lower color). Furthermore, it also appears that above a certain brightness, the color of IC 10 X-2 is roughly constant.

To determine the statistical significance of the relationship between color ($z_g - z_r$) and apparent magnitude z_g described above, we calculated their weighted correlation coefficient (WCC):

$$\text{WCC} = \frac{C_w(m, \Delta m, \sigma_m)}{\sqrt{C_w(m, m, \sigma_m) C_w(\Delta m, \Delta m, \sigma_m)}}, \quad (1)$$

where m is the apparent magnitude, Δm is the apparent color. M_w is the weighted mean:

$$M_w(m, \sigma_m) = \frac{\sum m \sigma_m}{\sum \sigma_m}, \quad (2)$$

and C_w is the weighted covariance:

$$C_w(m, \Delta m, M_w) = \frac{\sum \sigma_m (m - M_w)(\Delta m - M_w)}{\sum \sigma_m}. \quad (3)$$

For $z_g - z_r$, we find that when IC 10 X-2 is dimmer (apparent magnitude $z_g \geq 19.5$, the threshold for “flares” discussed in §3.3, WCC=0.73 – suggestive of a statistically significant correlation between color ($z_g - z_r$) and apparent z_g magnitude, while when IC 10 X-2 is brighter ($z_g < 19.5$), this correlation is significantly weaker or not present. These results are consistent with the observation discussed above, possible physical origins of this connection is discussed in §4.

3.3. Flare Identification and Properties

As mentioned in §3.1, we frequently detected variations in the apparent magnitude of IC 10 X-2 signifi-

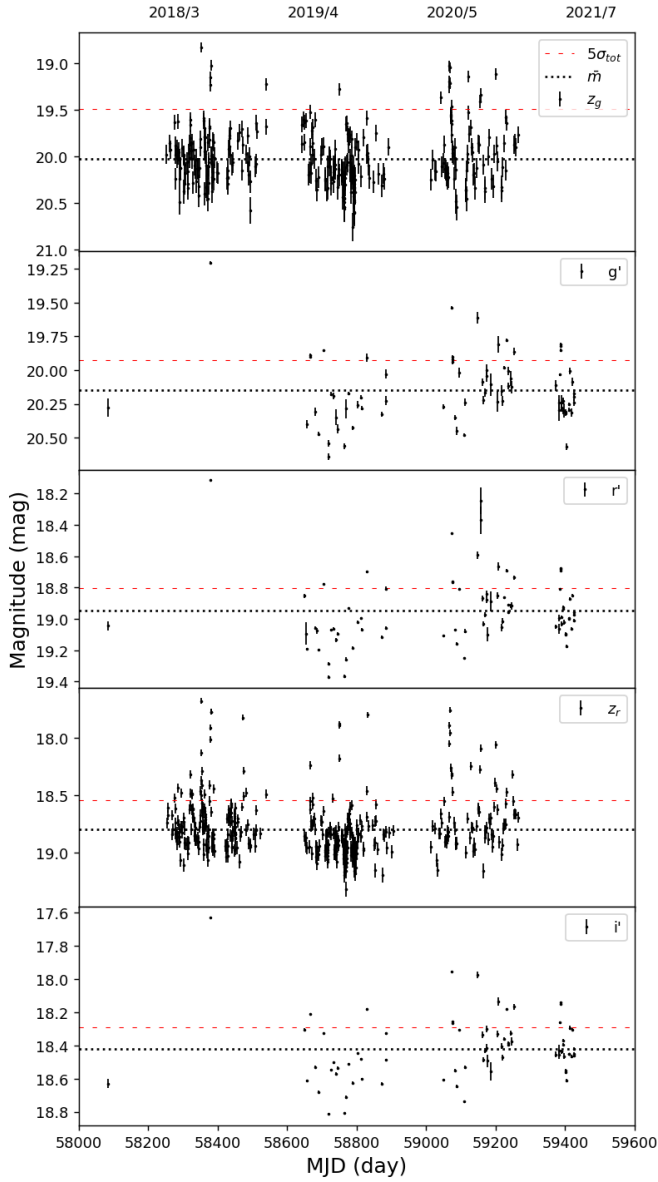


Figure 2. Apparent magnitude of IC 10 X-2 in g' , z_g , r' , z_r , and i' filters during the range of MJDs specified in Table 1. The dashed and dotted lines reflect the flare threshold (5σ) and average apparent magnitude \bar{m} , respectively, as calculated in §3.3.

cantly larger than the statistical error of individual measurements. Similar behavior in the optical and infrared emission of this source was previously reported by Kwan et al. (2018), who associated those epochs with an apparent magnitude 5σ smaller than average with “flares” from the source. We use a similar method to determine the threshold for flares for a particular filter in the observations analyzed here (Table 1), which we do by:

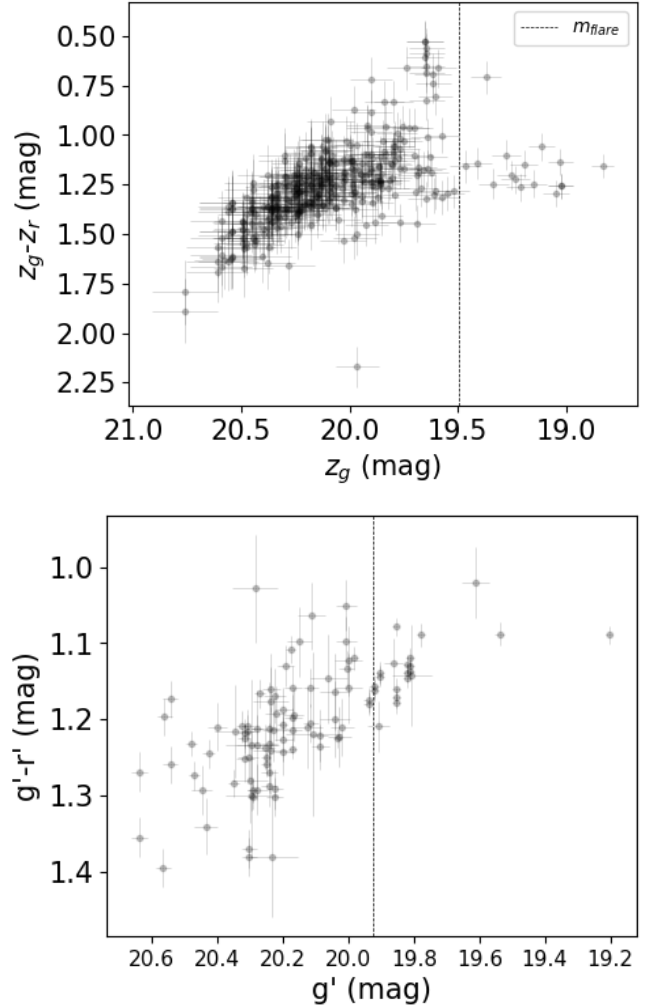


Figure 3. Observed color magnitude diagrams $z_g - z_r$ vs. z_g (top), and $g' - r'$ vs. g' (bottom) of IC 10 X-2. m_{flare} refers to the flare magnitude threshold calculated in §3.3.

1. fitting the light curve in a particular filter with a constant \bar{m} , which has an associated (statistical) uncertainty σ_{stat} ,
2. determine the (systematic) uncertainty in \bar{m} by calculating the average error in apparent magnitude, σ_{sys} , for all epochs where m is within $\bar{m} \pm 3\sigma_{\text{stat}}$,
3. calculate the total uncertainty in \bar{m} as:

$$\sigma_{\text{tot}} = \sqrt{\sigma_{\text{stat}}^2 + \sigma_{\text{sys}}^2}, \quad (4)$$

4. and, finally, set the flare magnitude threshold to be:

$$m_{\text{flare}} \equiv \bar{m} - 5\sigma_{\text{tot}}. \quad (5)$$

Table 4. Quantities used to calculate the magnitude threshold for IC 10 X-2 in the observed filters

Filter	\bar{m}	σ_{stat}	σ_{sys}	σ_{tot}	m_{flare}
...	mag	mag	mag	mag	mag
z_g	20.02	0.02	0.10	0.11	19.49
g'	20.15	0.03	0.03	0.04	19.93
r'	18.95	0.03	0.01	0.03	18.80
z_r	18.79	0.01	0.05	0.05	18.54
i'	18.42	0.02	0.01	0.03	18.29

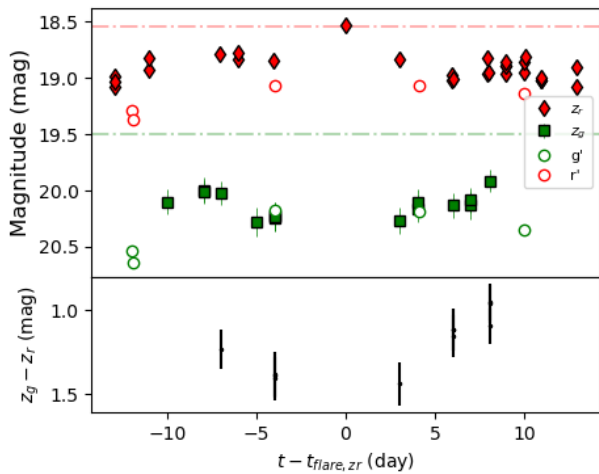


Figure 4. Multi-band light curve (*top*) and color (*bottom*) of IC 10 X-2 during W5 (Table 5).

The resultant values of these quantities for each of the observed filters are given in Table 4, and both \bar{m} and m_{flare} are indicated in the light curves shown in Figure 2.

As discussed in §3.4, the emission from IC 10 X-2 varies periodically with a period $P_{\text{orb}} \sim 26.5$ d. To identify when IC 10 X-2 exhibited flaring behavior, we defined a temporal window of width P_{orb} around each epoch with $m \leq m_{\text{flare}}$. We then merged together overlapping windows – resulting in several distinct episodes of flaring behavior listed in Table 5. As shown in Fig. 4, the detection of a flare during W5 was quite marginal, in contrast to the numerous strong flares during the other windows of activity as shown in Figure 5.

To measure the properties of these flaring episodes, we modeled the z_r light curve during each window (but

W5, due to a lack of data) as a sum of skew-normal functions¹

As mentioned in §3.2, the emission from IC 10 X-2 is observed to have a roughly constant value of $z_g - z_r$ when IC 10 X-2 is brighter than the flare threshold calculated above (Fig. 3). To quantify how well our z_r model reproduces the z_g emission during these Windows, we fit the z_g light-curve with the same functional form (Equation 6) and parameters (Table 5 derived from the z_r data, save for the quiescent magnitude m_q which was allowed to vary. The resultant values of m_q and χ^2 for z_g are reported in Table 5.

¹ whose implementation within `scipy` is described at <https://docs.scipy.org/doc/scipy/reference/generated/scipy.stats.skewnorm.html> plus a constant:

$$m(x) = \sum_i 2A_i \phi\left(\frac{x - \Delta t_i}{\sigma_i}\right) \Phi\left(a_i \frac{x - \Delta t_i}{\sigma_i}\right) + m_q \quad (6)$$

where:

- x is the time elapsed from the first z_r magnitude measurement in the window,
- ϕ is the Gaussian probability density function, and
- Φ is the cumulative distribution function of a Gaussian.

We used the non-linear least squares method, as implemented by the `curve_fit` function in SciPy, to determine the value of the following quantities

- A_i , the amplitude of a particular skew-normal component,
- Δt_i , the offset of a particular skew-normal component from the beginning of the window,
- σ_i , the width of a particular skew-normal component,
- a_i is the skewness parameter of a particular skew-normal component, and
- m_q , the quiescent z_r magnitude of IC 10 X-2 during this window.

which minimized the χ^2 , estimating the uncertainty of the fitted value of each parameter (σ) using the diagonal elements of the resultant covariance matrix. For each Window, we added skew-normal components until the fitted amplitude A_i became consistent within 3σ with zero ($A_i \leq 3\sigma_A$). Furthermore, we initially allowed the skewness a_i of each skew-normal component to vary, but in those cases where a_i was consistent with zero ($a_i \leq \sigma_a$), we set $a_i \equiv 0$ in order to minimize the number of model parameters. As listed in Table 5, a wide range of amplitudes (A_i), durations (width σ_i), and shape (skewness a_i) of the changes in magnitude were observed during these flaring episodes – with no significant correlations observed between the values of these different parameters.

Table 5. Values of the “best-fit” model parameters to the observed apparent magnitude of IC 10 X-2 during flaring “windows”, number of data points N , and model χ^2 , in each window

Window	Filter	t_{flare, z_r}	A	Δt	σ	a	m_q	N	χ^2
...	...	[MJD]	[mag]	[days]	[days]	...	[mag]
W1	z_r	58286.47	0.80 ± 0.20	-11.73 ± 0.49	2.59 ± 0.42	$\equiv 0$	18.83 ± 0.01	29	85.91
			0.80 ± 0.12	0.06 ± 0.25	0.49 ± 0.14	$\equiv 0$			
			0.80 ± 0.14	9.68 ± 0.30	0.79 ± 0.17	$\equiv 0$			
	z_g		20.07 ± 0.02	20	40.10
W2	z_r	58321.47	0.93 ± 0.13	-0.1 ± 0.11	0.80 ± 0.13	$\equiv 0$	18.96 ± 0.06	30	56.27
			0.91 ± 0.15	4.52 ± 0.55	5.80 ± 1.20	$\equiv 0$			
					
	z_g		20.22 ± 0.02	17	23.60
W3	z_r	58352.33	2.28 ± 0.76	1.85 ± 0.05	0.69 ± 0.15	-7.38 ± 4.33	18.93 ± 0.01	65	167.87
			0.98 ± 0.14	-0.31 ± 0.80	3.82 ± 0.66	1.34 ± 0.86			
			0.58 ± 0.07	10.58 ± 0.19	2.53 ± 0.39	3.22 ± 1.47			
			1.72 ± 0.06	30.21 ± 0.10	3.26 ± 0.16	-3.38 ± 0.45			
			0.60 ± 0.11	36.78 ± 7.31	0.62 ± 4.01	18.17 ± 0.01			
	z_g		20.15 ± 0.01	45	173.45
W4	z_r	58666.43	1.75 ± 0.09	0.09 ± 0.07	0.93 ± 0.07	$\equiv 0$	18.98 ± 0.02	25	59.68
			0.91 ± 0.07	8.35 ± 0.36	3.74 ± 0.48	$\equiv 0$			
			-			
	z_g		20.15 ± 0.03	13	54.43
W5	z_r	58730.4
	z_g	
W6	z_r	58751.33	1.79 ± 0.17	-0.15 ± 0.22	3.18 ± 0.26	2.30 ± 0.56	18.95 ± 0.01	38	85.48
	z_g		20.26 ± 0.03	20	50.30
W7	z_r	59068.38	1.38 ± 0.03	-0.44 ± 0.06	5.97 ± 0.22	8.41 ± 1.08	18.87 ± 0.02	21	46.60
	z_g		20.15 ± 0.02	26	53.55

As indicated in Table 5, this model resulted in fits with a reduced $\chi^2 \sim 1.5 - 4$. As shown in Figure 5, the largest deviations from the model are typically isolated data points – with a significant change in magnitude, often only in one filter (z_g or z_r), detected in $\sim 1 - 2$ epochs. These chromatic variations in the light curve could be indicative of variability on timescales shorter than the $\sim 0.5 - 1$ days separating observations in these filters. Such chromatic variations would result in significant changes in the color ($z_g - z_r$), and epochs whose color is $\gtrsim 3\sigma$ bluer / redder than quiescence during each window are indicated as blue / red points in the color panels of Figure 5. The possible nature of these variations will be discussed in §4.

3.4. Periodic Variability

To determine if there are periodic variations in the emission from IC 10 X-2, we calculated the Lomb-Scargle periodogram (Lomb 1976; Scargle 1982) of its observed z_g and z_r light curves. A commonly used technique for identifying periodic signals in light curves derived from unevenly spaced observations, in this method the apparent magnitudes are essentially fit with a model

(e.g., Equation 35 in VanderPlas 2018):

$$m(t; f) = A_f \sin(2\pi f(t - \phi_f)) \quad (7)$$

where f is the trial frequency of the periodic variations ($f \equiv 1/P$ where P is the period), where A_f and ϕ_f minimize the $\chi^2(f)$ of the fit at frequency f . The power \mathcal{P}_{psd} of a periodic signal with frequency f in the data is defined to be (e.g., Equation 37 in VanderPlas (2018)):

$$\mathcal{P}_{\text{psd}}(f) = \frac{1}{2}(\chi_{\text{ref}}^2 - \chi^2(f)), \quad (8)$$

where χ_{ref}^2 is the χ^2 resulting from performing such a fit on the “window,” or reference, function defined to be a constant magnitude at each observation epoch. Using the `LombScargle` class within `ASTROPY`, we searched for periodic modulations with a frequency $10^{-4} \leq f \leq 10 \text{ day}^{-1}$ ($0.1 \text{ days} \leq P \leq 10^4 \text{ days}$), using a samples per peak (number of trial frequency f across the Nyquist frequency derived from average spacing between observations) of 100. The resulting periodograms derived using all z_g and z_r observations are shown in Figure 6. Since frequency f is the only free parameter when calculating the periodogram, we define the 95% confidence

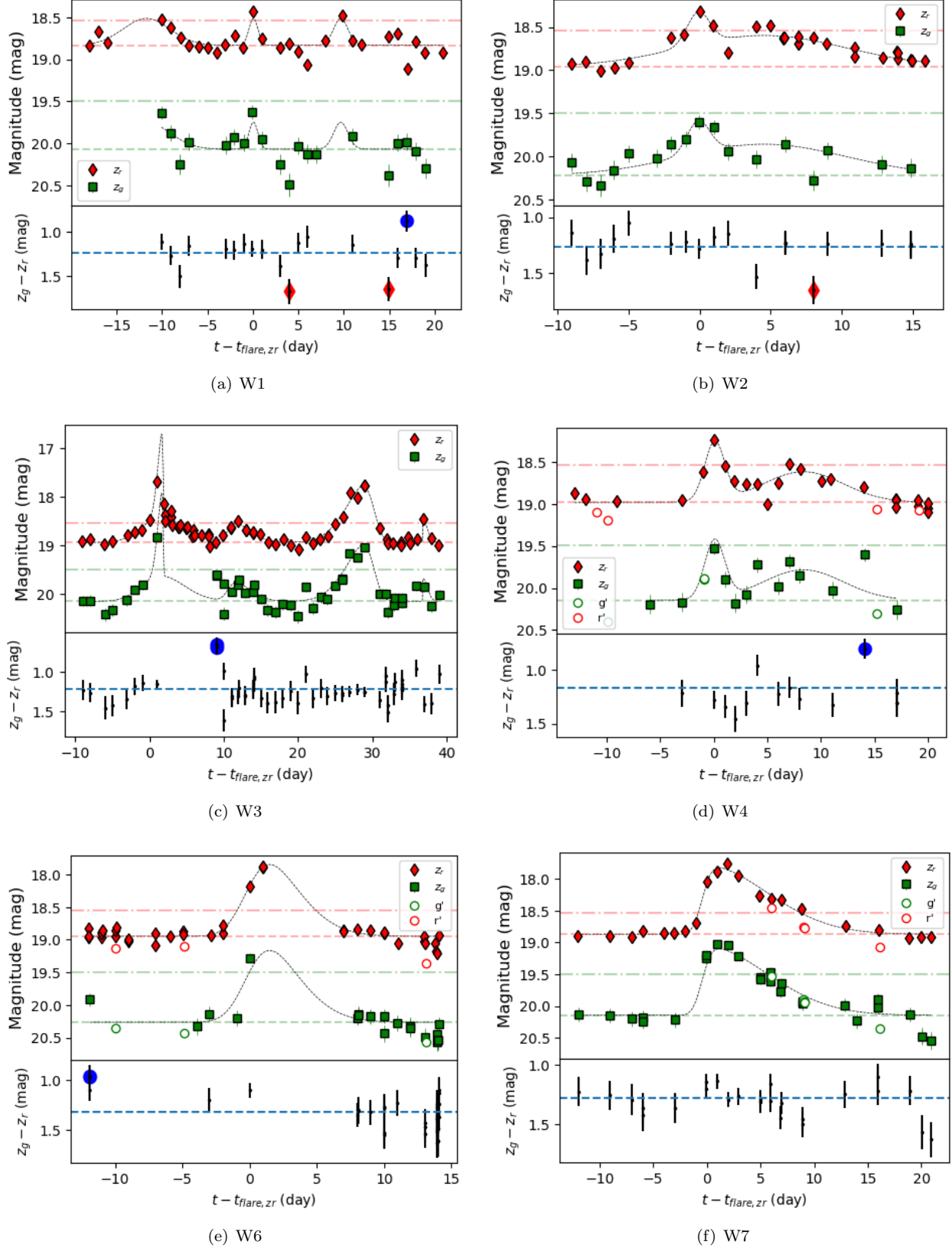


Figure 5. Apparent magnitude (*top* panel) and color (*bottom* panel) of IC 10 X-2 during each window of flaring activity described in §3.3. In the top panels, the solid lines indicate the skew-normal fits to the light curve (Table 5), the dashed lines indicate the quiescent magnitude m_q (Table 5) and the flare threshold m_{flare} (Table 4) for each filter. In the bottom panels, the dashed line indicates the quiescent color $m_{q,zg} - m_{q,zr}$, while epochs with color less / greater than 3σ of the quiescent color level are marked with blue circles / red diamonds, respectively.

interval on f_{\max} (P_{\max}) as the lowest and highest frequencies (periods) with power $\mathcal{P} > \mathcal{P}_{\max} - 1$ ($\Delta\chi^2 = 2$ relative to \mathcal{P}_{\max} ; Equation 8). The highest power \mathcal{P}_{psd} , corresponding frequency f_{\max} and period P_{\max} , and the uncertainty in these latter two quantities, are listed in Table 6.

Table 6. Properties of the periodic signal identified from the Lomb-Scargle analysis of the apparent magnitude of IC 10 X-2. All quantities are defined in §3.4

Filter	Flares?	$\mathcal{P}_{\text{FAL},99}$	\mathcal{P}_{\max}	f_{\max} 10^{-2}day^{-1}	P_{\max} days
z_g	Y	318.8	592.7	$3.768^{+0.002}_{-0.003}$	$26.54^{+0.02}_{-0.01}$
z_r	Y	1167.4	3063.1	$3.762^{+0.001}_{-0.001}$	$26.591^{+0.007}_{-0.007}$
z_g	N	78.24	77.65	$3.755^{+0.008}_{-0.007}$	$26.63^{+0.05}_{-0.06}$
z_r	N	202.3	540.9	$3.769^{+0.004}_{-0.003}$	$26.53^{+0.02}_{-0.03}$

As shown in Table 6, for both filters the maximum power \mathcal{P}_{\max} in the periodogram exceeds the 99% confidence false alarm level $\mathcal{P}_{\text{FAL},99}$, which for a periodogram with N trial frequencies, is the power which \mathcal{P} whose probability of occurring by chance is $1/(N \times 100)$, and the frequencies f_{\max} (period P_{\max}) corresponding to \mathcal{P}_{\max} agree to $\lesssim 10^{-3}$. Both $\mathcal{P}_{\max} > \mathcal{P}_{\text{FAL},99}$ and consistent values of f_{\max} (P_{\max}) strongly suggests the emission from IC 10 X-2 varies with a period of $P \sim 26.5$ days.

However, it is possible that this seeming periodicity is an artifact of the location of the IC 10 X-2 in the sky, and / or the cadence of these observations. To test the first scenario, we computed the periodogram of five ZTF z_r sources and four z_g sources $\lesssim 30''$, and with a similar number of observations and apparent magnitude, as IC 10 X-2. None of these sources show a statistically significant periodicity, let alone at $P_{\max} \sim 26.5$ days, arguing against the first possibility listed above.

To test the second possibility, we calculated the periodogram of the “window” function of the z_g and z_r observations of IC 10 X-2: a time series with the same MJD as the actual observations of IC 10 X-2, but each epoch has the same apparent magnitude. Since this is the reference function used in Equation 8, for this periodogram we computed the “standard” normalization of the power²:

$$\mathcal{P}_{\text{standard}}(F) \equiv \frac{\chi_{\text{ref}}^2 - \chi^2(f)}{\chi_{\text{ref}}^2} = \frac{2}{\chi_{\text{ref}}^2} \mathcal{P}_{\text{psd}}(F), \quad (9)$$

to more easily identify frequencies f where a periodicity may appear to occur simply due to the cadence,

² As defined by the `LombScargle` class in `ASTROPY`

Table 7. Frequencies ($f \text{ day}^{-1}$) with significant power in the periodograms (Figure 6).

z_g		z_r	
IC 10 X-2	Window	IC 10 X-2	Window
...	6.0030	...	6.0079
...	5.0026	...	5.0080
...	3.9999	...	4.0055
2.9678	3.0053	2.9705	3.0053
1.9651	2.0028	1.9678	2.0028
0.9650	1.0027	0.9651	1.0027
0.0376	...	0.0376	...

or spacing, of the observation. As shown in Figure 6, there are frequencies f with significant power which are listed in Table 7. In the “window” function, the frequencies with nearly (integer) frequencies f have significant power, and for $f \approx 1, 2, 3$ significant power is also observed in the periodogram of IC 10 X-2. However, the window function contains no evidence for a signal at $f \approx f_{\max}$ present in the periodogram of IC 10 X-2 (Figure 6, Table 7). We further tested the possibility of the observed f_{\max} being an artifact of the cadence of ZTF observations by randomizing the z_g and z_r light curves 10^4 times and calculating the resultant periodogram – with none of these randomized light curves having a \mathcal{P}_{\max} comparable to that observed in the actual light curve of IC 10 X-2. Therefore, based on these findings, we conclude that the observed ~ 26.5 day periodicity in the emission of IC 10 X-2 is intrinsic to the source and not an instrumental artifact of the ZTF observations.

To better study this periodicity, we folded the z_g and z_r light curves with a period $P = 26.54$ days (P_{\max} for the z_g data; Table 6) arbitrarily setting the phase at MJD 58084 (the date of the first LCO observation) $\phi_0 \equiv 0$. As shown in Figure 7, not only are measurements brighter than the flare threshold ($m < m_{\text{flare}}$) concentrated within a fairly narrow range of phases ($z_g, \phi \sim 0$ to $+0.2$; $z_r, \phi \sim -0.1$ to $+0.2$), there appears to be a sinusoidal variation in the apparent magnitude fainter than the flare threshold ($m > m_{\text{flare}}$) in both filters. We therefore fit the folded apparent magnitudes m with a sinusoidal function:

$$m(\phi) = A \sin(2\pi(\phi - \phi_0)) + m_q \quad (10)$$

where ϕ is phase (-0.5 to 0.5), A (mag) is the amplitude, and m_q (mag) is the midline magnitude. The resultant parameters are listed in Table 8. Folding the g' , r' , and i' light curves with the same 26.54 day period and ϕ_0 as found for z_r (Figure 8) finds a similar change in apparent magnitude with phase – magnitudes $m < m_{\text{flare}}$ are

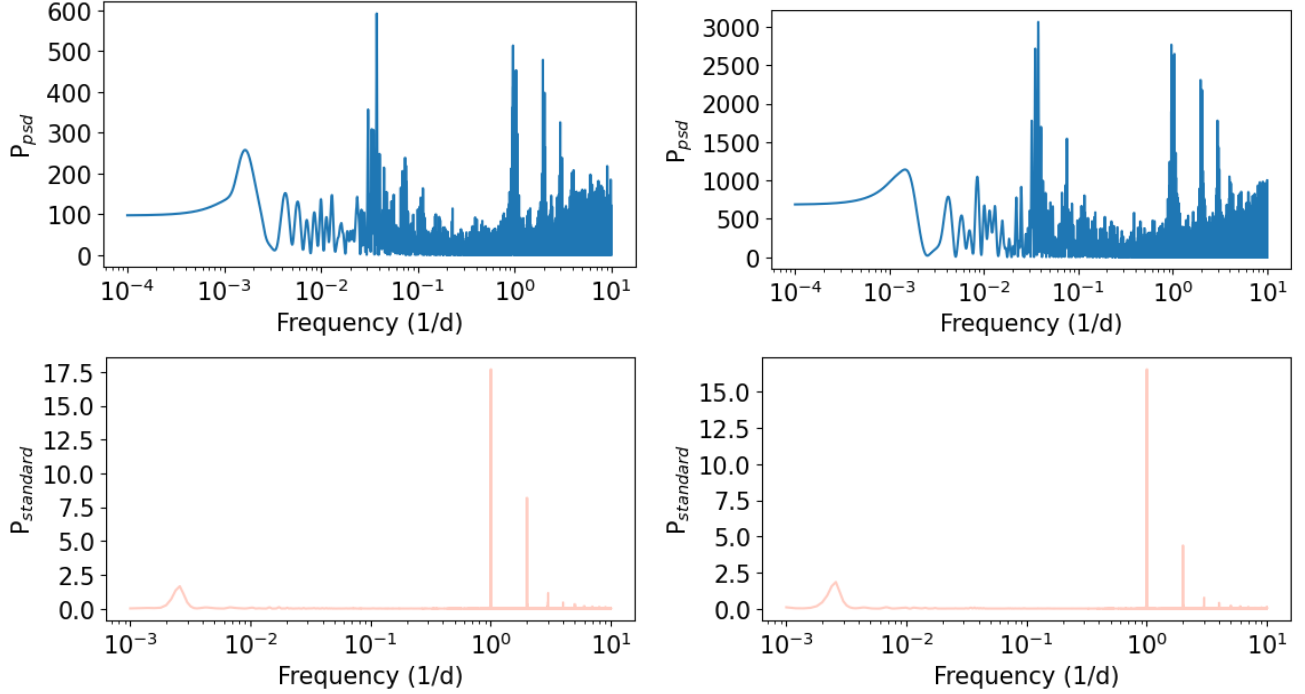


Figure 6. Lomb-Scargle periodograms of the measured z_g (left) and z_r (right) apparent magnitudes of this source (top row) and of the “window” functions as defined in §3.4 bottom row).

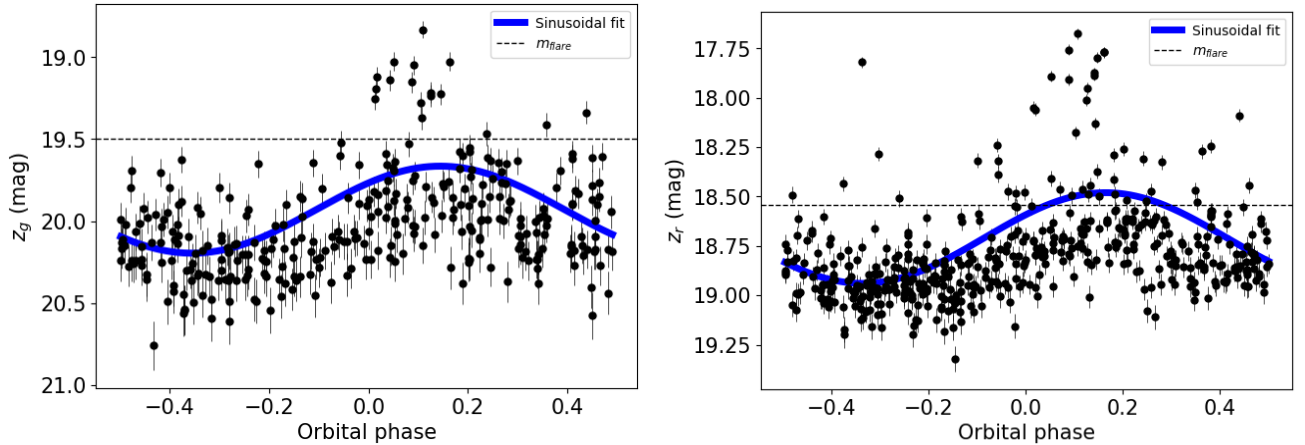


Figure 7. ZTF z_g (left) and z_r (right) light curves of IC 10 X-2 folded with on a $P = 26.54$ day period and phase $\phi(\text{MJD} = 58084) \equiv 0$. In both figures, the dotted horizontal line indicates the flare threshold (Table 4), and the thick blue line indicates a sinusoidal fit to the apparent magnitude as a function of orbital phase ϕ .

concentrated at phases $\phi \sim 0.2$, and IC 10 X-2 is fainter when $\phi < 0$ than $\phi > 0$. These results suggest that both the flaring and quiescent emission from IC 10 X-2 are periodic with the same $P \sim 26.54$ day timescale.

While formally the sinusoidal model (Equation 10) does not result in a good fit of the data, since the χ^2 is much greater than the degrees of freedom (dof; Table 8), as shown in Figure 7 this model appears to repro-

duce changes in the apparent magnitude of IC 10 X-2 when $m > m_{flare}$. To determine if the emission from IC 10 X-2 is periodic in its “quiescent” state, we calculated the periodogram of this source only using epochs where $m > m_{flare}$. As shown in Figure 9, the periodogram of the quiescent emission of IC 10 X-2 shows significant power ($\mathcal{P}_{psd} \gtrsim \mathcal{P}_{FAL,99}$) at frequencies f_{max} (period P_{max}) $< 1\%$ defined than observed in the full

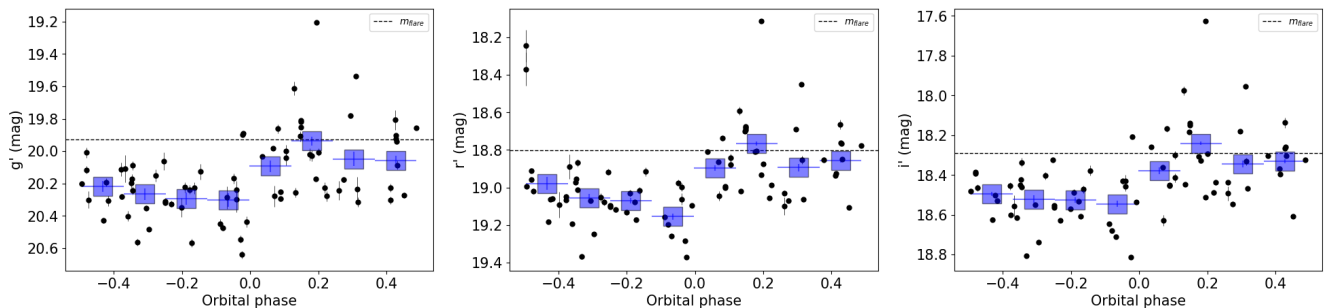


Figure 8. Light curves of g' , r' , and i' with flares folded with a period of 26.54 days and the value ϕ_0 derived from the folder z_r light curve (Table 8). The blue point indicate the binned folded light curve in these magnitudes.

Table 8. Model Parameters (Equation 10) derived from fitting the folded ZTF light curve of IC 10 X-2

Parameter	z_g	z_r
A	-0.265 ± 0.008	-0.230 ± 0.003
ϕ_0	0.105 ± 0.005	0.086 ± 0.002
m_q	19.930 ± 0.006	18.710 ± 0.002
χ^2 / dof	3122 / 320	17100 / 482

lightcurve of this source (Table 7). Therefore, we conclude that both the “quiescent” and flare emission from IC 10 X-2 periodically vary on a $P \sim 26.54$ d interval.

Finally, as shown in Table 8, the periodic oscillations in the z_g and z_r emission of IC 10 X-2 have a different amplitude A and phase ϕ_0 . As a result, we calculated the “quiescent” $z_g - z_r$ color of IC 10 X-2 as a function of phase ϕ assuming a 26.54 d period as above. The results are shown in Figure 10, which shows that the color does vary over this time period, with the reddest emission observed between phases ~ -0.5 to -0.2 while the bluest is at phases ~ 0 to 0.3 . Possible origins for periodic variations in color is described in this emission in §4.

4. DISCUSSION

In this Section, we discuss possible physical origins for the main results from the data analysis presented above:

1. in §4.1 presenting an interpretation for the constant color (§3.2), range in timescales (§3.3), and periodic nature (§3.4) of the long duration (multi-day) flares,
2. in §4.2 offer explanations for the color evolution (§3.2) and periodicity of the “quiescent” emission, and
3. in §4.3, the short time scale (\sim day) changes in the observed color (§3.2)

we observe from IC 10 X-2. This analysis is done within the context of previous studies of this source, which as

described in §1 found that IC 10 X-2 is a SFXT where a neutron star (NS) (Laycock et al. 2014) is orbiting a massive star – possibly a LBV (Kwan et al. 2018). In such a system, the optical and near-IR emission studied is likely to be dominated by the massive star and/or material accreting onto the NS.

Before calculating the properties of IC 10 X-2, it is necessary to convert the apparent magnitudes measured in these observations to the absolute magnitude M_F intrinsic to the source:

$$M_F = m_F - A_F - \mu \quad (11)$$

where μ is the distance modulus to IC 10 ($\mu \sim 24$; Kim et al. 2009; Laycock et al. 2014) and A_F is the extinction along the line of sight for a particular filter F . The value of A_F depends on the total Hydrogen column density N_H towards IC 10 X-2, the properties of the absorbing material – which relates N_H to A_V , extinction in the visual V band – and extinction constant y – which relates A_V to A_F . From the X-ray spectrum of IC 10 X-2, Laycock et al. (2014) measured that a total $N_H^{\text{tot}} = 6.3 \times 10^{21} \text{ cm}^{-2}$, which is combination of material in the Milky Way, in the foreground interstellar medium of IC 10, and within IC 10 X-2 itself. Galactic HI surveys suggest that, along this line of sight, within the Milky Way (MW) $N_H^{\text{MW}} \approx 5.1 \times 10^{21} \text{ cm}^{-2}$ (HI4PI Collaboration et al. 2016; Kalberla et al. 2005; Dickey & Lockman 1990), and therefore responsible for $\sim 80\%$ of the total extinction observed towards this source. As a result, we estimate A_V^{tot} using the $N_H - A_V$ relation derived for MW dust (Bohlin et al. 1978; Foight et al. 2016; Zhu et al. 2017; Whittet 2022):

$$A_V^{\text{tot}} \approx \frac{N_H^{\text{tot}}}{2.1 \times 10^{21} \text{ cm}^{-2}} \text{ mag} \approx 3 \text{ mag}. \quad (12)$$

The extinction in a filter A_F is then:

$$A_F = y_F \times A_V \quad (13)$$

where y_F is the extinction constant provided by the SVO Filter Service (Rodrigo et al. 2012; Rodrigo & Solano

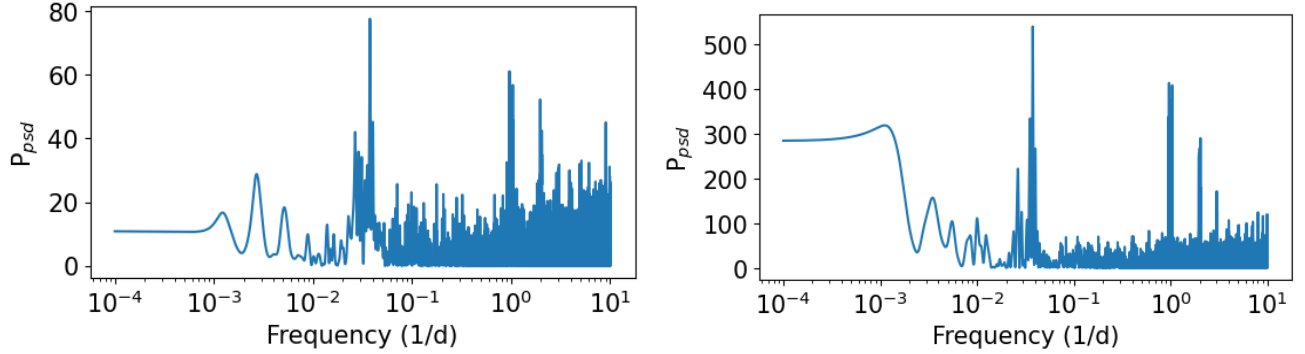


Figure 9. Lomb-Scargle periodograms of the measured z_g (left) and z_r (right) apparent magnitudes of IC 10 X-2 on including epochs where $m > m_{\text{flare}}$ (“quiescent” emission).

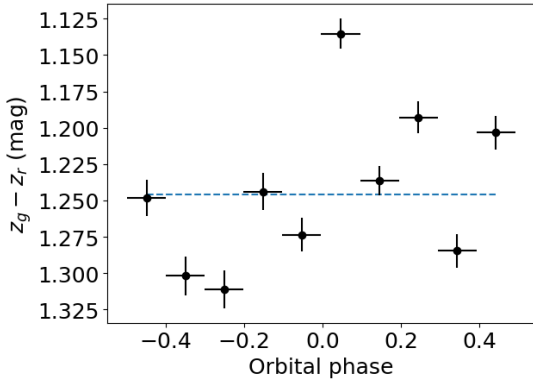


Figure 10. Average observed $z_g - z_r$ color of IC 10 X-2 for phase bins for a 26.54 d period. The dashed horizontal line indicates the best-fit constant color of this source.

Table 9. Extinction constant y , extinction magnitude A_F , and quiescent absolute magnitude $M_{q,F}$ of IC 10 X-2

Filter	y	A_F	$M_{q,F}$
...	...	mag	mag
g'	1.21	3.63	-7.3
z_g	1.19	3.57	-7.6
r'	0.878	2.63	-7.5
z_r	0.834	2.50	-7.8
i'	0.669	2.00	-7.5

2020). The values of y_F , A_F , and resultant absolute “quiescent” magnitude $M_{q,F}$ of IC 10 X-2 for all of the filters used in this work are provided in Table 9.

4.1. Nature of Long Duration Flares

As mentioned above, our analysis suggests that IC 10 X-2 periodically (§3.4) produces flares ($m < m_{\text{flare}}$) which last $\gtrsim 1-6$ days (§3.3, Table 5) during which the color of this source is roughly constant (§3.2). As discussed in §1, periodic flaring is a signature of BeHMXBs

– and therefore treat IC 10 X-2 as a member of this source class. We note that this is not inconsistent with the previous classifications of IC 10 X-2 as a SFXT (Laycock et al. 2014) or having a LBV companion (Kwan et al. 2018), since both have been associated BeHMXBs (e.g., Bird 2012; Clark et al. 2013; Liu et al. 2011). Furthermore, the absolute magnitude of IC 10 X-2 is similar to that of luminosity class Ia OeBe stars (e.g., Wegner 2006), supporting this identification.

In this scenario, the observed flares are result of the NS penetrating the clumpy decretion disk produced by its supergiant stellar companion, resulting in an increase in the accretion rate of material onto the NS. Therefore, the period of the flares is likely the orbital period P_{orb} of the binary system that constitutes IC 10 X-2 $P_{\text{orb}} \sim 26.5-26.6$ d (§3.4, Table 6) – which is very similar to the orbital period of other BeHMXBs (Fortin et al. 2023), such as LS I+61°303 ($P_{\text{orb}} \approx 26.5$ d; Gregory 2002). Furthermore, the emission observed during these flares is likely dominated by material accreting onto the NS. The expected hot temperature $T \sim 10^6$ K of this material suggests that, at the wavelengths of these observations (Table 1), the observed emission would fall within the Rayleigh-Jeans regime of the resultant blackbody radiation. In this case, the frequency dependence ν of the emitted flux density \mathcal{S}_ν should be $S_\nu \propto \nu^2$, which correspond to an unextincted color of:

$$(z_g - z_r)_0 \approx -0.64 \quad (14)$$

$$(g' - r')_0 \approx -0.57, \quad (15)$$

significantly bluer than the $(z_g - z_r)_{\text{obs}} \approx 1.25$ and $(g' - r') \approx 1.1$ observed during these flares. The natural explanation for this discrepancy is that it is due to extinction A_ν along the line of sight which, from Equations

11 & 13, is equal to:

$$A_V^{z_g - z_r} = \frac{(z_g - z_r)_{\text{obs}} - (z_g - z_r)_0}{y_{z_g} - y_{z_r}} \approx 5.31 \quad (16)$$

$$A_V^{g' - r'} = \frac{(g' - r')_{\text{obs}} - (g' - r')_0}{y_{g'} - y_{r'}} \approx 5.03 \quad (17)$$

for the y values given in Table 9 – two magnitudes of extinction more than inferred in Equation 12. This suggests that, during the flares, the Hydrogen column density towards material accreting on to the NS is $N_{\text{H}}^{\text{flare}} \sim 10^{22} \text{ cm}^{-2}$. This increase in N_{H} during the flare could lead to a decrease and hardening of the X-ray emission produced during this period, as observed previously from this source (Laycock et al. 2014), and similar changes and values of N_{H} have been observed in other HMXBs (e.g., IGR J17544–2619; González-Riestra et al. 2004). A test of this hypothesis would be synchronous optical and UV / X-ray observations of this source, to see if optical flares are indeed associated with increases in extinction as observed in other bands.

Lastly, the duration of these flares would be connected to the duration of the increased accretion onto the NS, which should occur when it is within the decretion disk. Therefore, the ratio of the flare duration to orbital period provides an estimate of the fraction of the NS’s orbit spend inside this structure. As listed in Table 5, most windows contain at least one flare $\sigma \gtrsim 2.5$ days long, suggesting that the decretion disk encompasses $\gtrsim 10\%$ of the NS’s orbit. This has implications for the eccentricity of the NS’s orbit, as well as the extent and thickness of the decretion disk produced by the stellar companion, which require additional information to disentangle.

4.2. Periodicity and Color Evolution of Quiescent Emission

As demonstrated above, our analysis of these observations of this source suggests that, not only does the quiescent emission vary in intensity on the same timescale as the orbital period P_{orb} (§3.4, Table 6), its color changes as well – with the quiescent emission being “bluer” when it is brighter (§3.2, Figure 3). This is opposite to what is observed in many other BeXRBs, where the optical emission is redder when brighter (e.g., Swift J0549.7-6812, Monageng et al. 2019; RX J0123.4-7321, Coe et al. 2021; Swift J010745.0-722740, Schmidtke et al. 2021; RX J0529.8-6556 Treiber et al. 2021; XMMU J010331.7-730144, Monageng et al. 2020; SXP 91.1, Monageng et al. 2019; Swift J010902.6-723710, Gaudin et al. 2024). In these systems, the optical reddening and increase in brightness are believed to result in a scenario similar to that discussed in §4.1 – the passage of the NS through the decretion disk leads to increased accretion,

increasing its brightness, and increased absorption along the line of sight, reddening the observed emission. Since we observe IC 10 X-2 to be “bluer” when brighter, a different explanation is required. Below, we discuss two possible explanations for the color-magnitude behavior of IC 10 X-2: changes in extinction through the decretion disk with orbital phase (§4.2.1), and the formation of a transient accretion disk around the NS (§4.2.2) as it passes through the stellar decretion disk.

4.2.1. Orbital Variations in Extinction

As detailed in §3.3, IC 10 X-2 is likely a BeHMXB where the powerful stellar winds of the massive star companion generate a decretion disk. Depending on the geometry of the system, the line of sight to the massive star passes through its decretion disk, which will contribute to the total Hydrogen column density N_{H} towards the stellar companion. The interaction between the neutron star and decretion disk is expected to produce density inhomogeneities in the disk (e.g., Manousakis & Walter 2015a), which results in variations in N_{H} through the disk over the orbital period of the neutron star (e.g., Manousakis & Walter 2011, 2015b). In this model, we posit that the “quiescent” emission is dominated by radiation from the stellar companion and that the observed changes in brightness and color of this emission are due to changes in Hydrogen column density $\Delta N_{\text{H}}^{\text{orb}}$ towards the star over the orbit.

To calculate $\Delta N_{\text{H}}^{\text{orb}}$ due to obscuring material within IC 10 X-2, we first need to determine the conversion between N_{H} and A_{F} , which depends on the physical properties of the internal material. These quantities also determine the constant R relationship and the change in magnitude to that in color due to the passage of light through the absorbing material:

$$A_{\lambda_1} = R_{\lambda_1} E(\lambda_1 - \lambda_2) \quad (18)$$

where $E(\lambda_1 - \lambda_2)$ is the reddening between observations at wavelengths λ_1 and λ_2 . Since the LCO data is significantly more precise than that collected by ZTF, we use this dataset to calculate R .

In this scenario, the quiescent emission is bluest and brightest when the extinction along the line of sight A_{F} is at a minimum. From Figure 3, we estimate that, at this time (Figure 3):

$$m_{g'}^{\text{bluest}} \sim 19.54 \text{ mag, and} \\ (g' - r')_{\text{bluest}} \sim 1.02 \text{ mag.}$$

Therefore, at a given time t , the change in extinction $\Delta A_{g'}(t)$ and reddening $\Delta E(g' - r'; t)$ towards the stellar component of IC 10 X-2 due to the intrasystem material

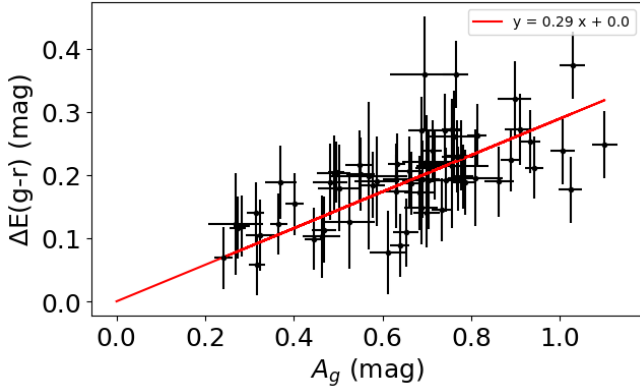


Figure 11. The color excess $\Delta E(g' - r')$ against observed extinction $\Delta A_{g'}$, with the best fit linear relation between these two parameters (red line).

Table 10. Model Parameters (Equation 10) derived from fitting the folded “quiescent” ZTF light curve of IC 10 X-2

Parameter	z_g	z_r
A	-0.16 ± 0.01	-0.11 ± 0.0
ϕ_0	0.06 ± 0.01	0.04 ± 0.0
m_q	20.01 ± 0.01	18.82 ± 0.0
χ^2 / dof	1337 / 303	2530 / 432

is:

$$\Delta A_{g'}(t) = m_{g'}(t) - m_{g'}^{\text{bluest}} \quad (19)$$

$$\Delta E(g' - r'; t) = (g' - r')(t) - (g' - r')_{\text{bluest}}. \quad (20)$$

As expected, $\Delta E(g' - r')$ appears to increase for larger values of $\Delta A_{g'}$ (Figure 11). We use a least-squares-minimization routine to fit a line to these parameters, with $R_{g'}^{\text{orb}}$ of the absorbing material being the inverse of the resultant slope following Equation 18). This analysis suggest that the material inside IC 10 X-2 has $R_{g'}^{\text{orb}} \sim 3.5$, similar to the value measured for MW dust ($R_{g'}^{\text{MW}} \sim 3.3$; Yuan et al. 2013). Therefore, the relation between N_{H} and A_{V} derived for MW dust (Equation 12) should be a good approximation for the absorbing material within IC 10 X-2.

The next step in calculating $\Delta N_{\text{H}}^{\text{orb}}$ is determining the extinction $\Delta A_{\text{V}}^{\text{orb}}$ during an orbit – which in this interpretation is related to the amplitude A of the periodic oscillations in the quiescent emission. To do so, we fit the folded z_g and z_r light curve with the same model used in §3.4 (Equation 10, but only using data points with $m > m_{\text{flare}}$ (Table 4), which results in the parameters listed in Table 10. We calculate $\Delta A_{\text{V}}^{\text{orb},F}$ using the

equation:

$$\Delta A_{\text{V}}^{\text{orb},F} = \frac{2}{y_{\text{F}}} |A_{\text{F}}|, \quad (21)$$

where A_{F} is the amplitude of the sinusoidal variations, and y_{F} is the extinction coefficient (Table 9), for filter F . For amplitudes A measured from the z_g and z_r folded light curves given in Table 10, we have:

$$\Delta A_{\text{V}}^{\text{orb},z_g} \approx 0.27 \text{ mag}, \text{ and} \quad (22)$$

$$\Delta A_{\text{V}}^{\text{orb},z_r} \approx 0.26 \text{ mag}. \quad (23)$$

From Equation 12, we therefore have:

$$\Delta N_{\text{H}}^{\text{orb}} \sim 5.5 \times 10^{21} \text{ cm}^{-2}, \quad (24)$$

a quantity $\sim 1/2$ of the $N_{\text{H}}^{\text{flare}}$ during the long duration flares which occur when the neutron star is embedded in the thickest part of the decretion disk (§4.1). This value is smaller than inferred from other systems – possibly the result of differences in the stellar wind and observing geometry (e.g., Manousakis & Walter 2011, 2015b).

4.2.2. Transient accretion disk

In this section, we investigate the possibility that the observed periodic oscillations in the “quiescent” emission is the result of a transient accretion disk around the neutron star. As the neutron star orbits its massive star companion, it is expected to accrete material from its surroundings. This material will likely be hotter, and therefore its emission will be “bluer,” than the stellar companion. Furthermore, the intensity of the emission is likely to vary over the neutron star’s orbit due to changes in the surrounding density, and the timescale with which captured material falls onto the neutron star. When the intensity of emission from the disk grows, its increased contribution to the total emission from the system will make it appear brighter and bluer, as observed. Therefore, a “transient” accretion disk – as observed in other systems similar to IC 10 X-2 (e.g., Ducci et al. 2010)– could also explain the periodic changes in brightness and color of the “quiescent” emission discussed in §3.4.

Whether or not a transient accretion disk will form in a HMXB (e.g., Hainich et al. 2020) depends on the properties of the NS, its orbit, and the wind produced by its SG companion. As an initial approximation of the orbital parameters, we assume the NS and SG are moving in circular orbits of radius d_{NS} and d_{SG} , respectively, around their mutual center of mass, such that the total distance d_{tot} between them:

$$d_{\text{tot}} = d_{\text{NS}} + d_{\text{SG}} \quad (25)$$

is constant with time. In the simplifying case of a circular orbit, we have:

$$d_{\text{SG}} = \frac{d_{\text{tot}} M_{\text{NS}}}{M_{\text{SG}} + M_{\text{NS}}} \quad (26)$$

$$v_{\text{SG}} = \sqrt{\frac{G M_{\text{NS}} d_{\text{SG}}}{d_{\text{tot}}^2}} \quad (27)$$

$$v_{\text{NS}} = \sqrt{\frac{G M_{\text{SG}} d_{\text{NS}}}{d_{\text{tot}}^2}} \quad (28)$$

$$P = \frac{2\pi d_{\text{SG}}}{v_{\text{SG}}} \quad (29)$$

$$d_{\text{tot}} = \left(\frac{P}{2\pi}\right)^{\frac{2}{3}} [G(M_{\text{SG}} + M_{\text{NS}})]^{\frac{1}{3}}, \quad (30)$$

where G is the gravitational constant. For a SG mass $M_{\text{SG}} = 21.5 M_{\odot}$ and NS mass $M_{\text{NS}} = 1.5 M_{\odot}$, as used by Kwan et al. 2018, this results in:

$$\begin{aligned} d_{\text{tot}} &\approx 7.2 \times 10^{12} \text{ cm}, \\ d_{\text{SG}} &\approx 5.1 \times 10^{11} \text{ cm}, \text{ and} \\ d_{\text{NS}} &\approx 6.7 \times 10^{12} \text{ cm}. \end{aligned}$$

We note that, given the typical radius of SG stars ($R_{\text{SG}} \sim 10 R_{\odot} = 7 \times 10^{11} \text{ cm}$; Karino et al. 2019), the center of mass of this system likely located near the edge of the stellar companion.

As shown in Figure 12, stellar wind material when passes within a distance r_{acc} of the NS will be captured, and eventually accreted, onto the compact object. This distance is approximated as where, relative to the NS, the potential and kinetic energy of the stellar wind material are equivalent (Karino et al. 2019):

$$\begin{aligned} r_{\text{acc}} &= \left(\frac{2 G M_{\text{NS}}}{v_{\text{rel}}^2}\right) \\ &= 4.7 \left(\frac{M_{\text{NS}}}{1.5 M_{\odot}}\right) \left(\frac{v_{\text{rel}}}{900 \text{ km/s}}\right)^{-2} \times 10^{10} \text{ cm} \end{aligned} \quad (31)$$

where G is the gravitational constant, v_{rel} is the relative velocity, at the location of the NS d_{NS} , between the stellar wind v_w and the NS v_{ns} . Following work done by Karino et al. (2019), we approximate v_{rel} as:

$$v_{\text{rel}}^2 = v_w^2 + v_{\text{NS}}^2. \quad (32)$$

To determine the speed of the stellar wind v_w , we use the profile presented by Karino et al. 2019 among others, where:

$$v_w = v_{\infty} \left(1 - \frac{R_{\text{SG}}}{d_{\text{NS}}}\right)^{\beta}. \quad (33)$$

For an acceleration parameter $\beta = 1$, and a wind speed at $r = \infty$ of $v_{\infty} = 10^5 \text{ km s}^{-1}$ (e.g., Karino et al. 2019),

we find $r_{\text{acc}} \approx 4.7 \times 10^{10} \text{ cm}$ – a small fraction of the distance between the NS and SG.

Stellar wind material entering within r_{acc} of the NS provides an influx of angular momentum J and mass M , which eventually accretes on the NS. For wind-fed X-ray binaries like IC 10 X-2, whether or not this material forms a disk around the NS depends requires that both (e.g., Karino et al. 2019):

1. the circularization radius r_{circ} , defined to be the distance from the NS where the initial angular momentum of the accreting material is equal to the angular momentum of a circular orbit around the NS, and
2. and the co-rotation radius r_{co} , the distance from the NS where the period of a circular orbit is the same as its spin period,

of the accreting material are larger than the neutron star's magnetospheric's radius r_m , the distance from the NS where the accretion disk is disrupted by the NS's surface magnetic field (Karino et al. 2019):

$$r_m < r_{\text{co}}, r_{\text{circ}}. \quad (34)$$

As described by Karino et al. (2019), the circularization radius r_{circ} is:

$$r_{\text{circ}} = \frac{l^2}{G M_{\text{NS}}} \quad (35)$$

where l is the specific angular momentum of stellar wind material captured by the neutron star:

$$l = \frac{\dot{J}}{\dot{M}} \quad (36)$$

where \dot{J} and \dot{M} are, respectively, the rate at which angular momentum and mass from stellar wind material cross the boundary $r = r_{\text{acc}}$ from the NS (e.g., Karino et al. 2019). Using the coordinate system defined in Figure 12, these can be approximated as (Karino et al. 2019):

$$\begin{aligned} \dot{J} &\approx r_{\text{acc}} \rho_w v_w^2 \int_0^{\pi/2} \int_0^{\pi} \sin^2 \theta \cos \theta d\theta d\varphi \\ &\approx \frac{2}{3} \pi r_{\text{acc}}^3 \rho_w v_w^2 \end{aligned} \quad (37)$$

and

$$\dot{M} \approx \dot{M}_w \frac{r_{\text{acc}}^2}{4 d_{\text{NS}}^2} \quad (38)$$

where ρ_w is the SG wind material density at d_{NS} . Assuming conservation of mass flux, ρ_w is approximately

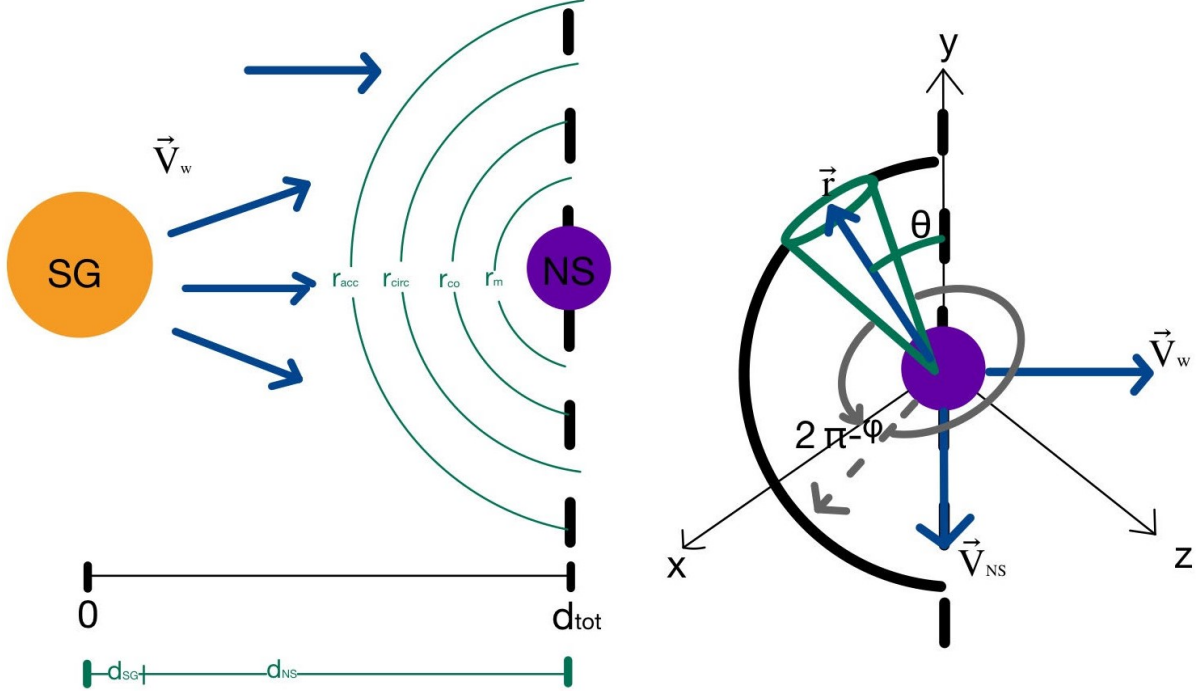


Figure 12. An illustration of IC 10 X-2 system geometry (see text for variables’ definition)

(e.g., Karino et al. 2019):

$$\rho_w = \frac{\dot{M}_w}{4\pi d_{NS}^2 v_w}, \quad (39)$$

which results in:

$$r_{circ} = \frac{2}{3} \frac{r_{acc}}{v_w} \quad (40)$$

$$\sim 4 \times 10^{10} \text{ cm}, \quad (41)$$

roughly $\sim 80\%$ of r_{acc} calculated above.

Not surprisingly, The corotation radius depends on the unknown spin period P_{spin} of the NS (e.g., Karino et al. 2019):

$$r_{co} = \left(\frac{G M_{NS} P_{spin}^2}{4\pi^2} \right)^{\frac{1}{3}} \quad (42)$$

$$\approx 3.7 \left(\frac{G M_{NS}}{4\pi^2 1.5 M_{\odot}} \right)^{\frac{1}{3}} \left(\frac{P_{spin}}{100 \text{ s}} \right)^{\frac{2}{3}} \times 10^9 \text{ cm}$$

which is currently unknown for the NS believed to be located in IC 10 X-2. As shown in Table 11, $r_{co} < r_{circ}$ even for extremely long spin periods – suggesting this quantity will determine if a transient accretion disk is capable of forming in IC 10 X-2.

Lastly, we calculate the magnetospheric radius r_m , which as derived by Karino et al. (2019) depends not

only on the mass M_{NS} , radius R_{NS} , and surface magnetic field strength B_{NS} of the neutron star, but also the mass loss rate of the stellar companion \dot{M}_w and efficiency ξ of accretion onto the NS (e.g., Karino et al. 2019):

$$r_m = \left(\frac{B_{NS}^4 R_{NS}^{12}}{8\xi^2 G M_{NS} \dot{M}_w^2} \right)^{\frac{1}{7}},$$

$$= 7.2 \left(\frac{B_{NS}}{2 \times 10^{12} \text{ G}} \right)^{\frac{4}{7}} \left(\frac{R_{NS}}{10^6 \text{ cm}} \right)^{\frac{12}{7}} \left(\frac{\xi}{0.5} \right)^{-\frac{2}{7}} \quad (43)$$

$$\left(\frac{M_{NS}}{1.5 M_{\odot}} \right)^{-\frac{1}{7}} \left(\frac{\dot{M}_w}{10^{-6} \frac{M_{\odot}}{\text{yr}}} \right)^{-\frac{2}{7}} \times 10^7 \text{ cm}.$$

While the range of possible values for most of these parameters is small (less than an order of magnitude), \dot{M}_w ranges from $\sim 10^{-7} M_{\odot} \text{ yr}^{-1}$ in Be stars (e.g., Lamers & Cassinelli 1999) to a “typical” value of $\sim 10^{-6} M_{\odot} \text{ yr}^{-1}$ in massive stars (e.g., Kudritzki & Puls 2000) to $\sim 10^{-4} M_{\odot} \text{ yr}^{-1}$ in red supergiants (e.g., Maunon, N. & Josselin, E. 2011). However, as shown in Table 11, across this range r_m is $\lesssim 0.1 r_{co}$ – suggesting that a transient accretion disk can form in IC 10 X-2 per the criterion specified in Equation 34.

However, if a transient accretion disk is indeed responsible for the periodic oscillations in the emission observed from IC 10 X-2, then the luminosity of these variations $L_{opt,disk}$ must be smaller than the total ra-

Table 11. Physical properties of transient accretion disk, for different values of \dot{M}_w and P_{spin} , assuming circular orbits.

P_{spin} [s]	10	100	1000
r_{co} [cm]	8.0×10^8	3.7×10^9	1.7×10^{10}
\dot{M}_w [$\frac{M_\odot}{yr}$]	10^{-7}	10^{-6}	10^{-4}
ρ_w [$\frac{g}{cm^3}$]	1.2×10^{-16}	1.2×10^{-15}	1.2×10^{-13}
\dot{M} [$\frac{M_\odot}{yr}$]	1.2×10^{-12}	1.2×10^{-11}	1.2×10^{-9}
j [$g \frac{cm^2}{s^2}$]	2.2×10^{32}	2.2×10^{33}	2.2×10^{35}
r_m [cm]	1.4×10^{-8}	7.2×10^7	1.90×10^7

diative luminosity generated by accretion onto the NS L_{acc} :

$$L_{acc} \equiv \eta \dot{M} c^2, \quad (44)$$

where η is the radiative efficiency of the accreting matter. The amplitude of the oscillations derived from fitting the folded quiescent light curve (Table 10) suggests that, in the observed bands these oscillations have $\nu L_\nu \sim 4 \times 10^{37}$ ergs s^{-1} . While the relative amplitude of the oscillation in quiescent emission observed in the different filters studied in this work is consistent with the $L_\nu \propto \nu^2$ expected from the Rayleigh-Jeans tail of a multi-temperature blackbody radiation as expected from an accretion disk heated by primarily viscous forces (e.g., Shakura & Sunyaev 1973; Frank et al. 2002; Russell et al. 2008), the errors are sufficiently large to preclude modeling of this SED. Therefore, we approximate $L_{opt,disk} \sim 4 \times 10^{37}$ ergs s^{-1} . Requiring $L_{opt,disk} \leq L_{acc}$ therefore requires:

$$\dot{M} \geq 8 \left(\frac{\eta}{0.1} \right)^{-1} \times 10^{-10} \frac{M_\odot}{yr}. \quad (45)$$

From the calculations above, assuming a circular orbit, this requires the SG companion expels $\dot{M} \gtrsim 7.5 \times 10^{-5} M_\odot yr^{-1}$ for $\eta \sim 0.1$ – mass loss rates more characteristic of red supergiants (e.g. Mauron, N. & Josselin, E. 2011) than the Be star (e.g., Lamers & Cassinelli 1999; Kudritzki & Puls 2000) expected to reside in IC 10 X-2.

It is possible that, if the orbits in IC 10 X-2 are eccentric – as observed from most BeHMXBs (e.g., Kretschmar et al. 2019) – lower values of \dot{M}_w are potentially possible. If the NS enters the decretion disk during an orbital phase near periaapsis, the NS will be closer to the SG, and moving faster, than in the case of a circular orbit. This will increase both the velocity of the NS relative to the stellar wind (v_{rel}) and the density of the stellar wind (ρ_w) when the NS enters the decretion disk, leading to an increase in \dot{M} onto the NS. However, it is

unclear the minimum stellar mass rate \dot{M}_w capable of producing an accretion rate onto the NS \dot{M} sufficient to power the quiescent oscillations.

4.3. Short timescale color variability

As discussed in §3.2, we also observed that, on several occasions, that IC 10 X-2 gets significantly bluer or redder for a short ($\lesssim 1$ day) period of time (Figure 5). The short timescales of these event suggests the existence of small scale structures – either over dense or under dense regions – in this system. There are multiple possible origins for clumps and holes (e.g., Kretschmar et al. 2019) inside a sgHMXB such as IC 10 X-2 including instabilities in the stellar winds itself (e.g., Martínez-Núñez et al. 2017) and the interaction between the NS and the decretion disk (e.g., Manousakis & Walter 2015a; El Mellah et al. 2018).

One possible explanation for IC 10 X-2 getting “redder” is increased absorption resulting from a dense clump passing through the line of sight towards the main source of optical and infrared emission (which is believed to be the SG star). Following the analysis of §4.1, we can estimate the change in extinction ΔA_V^{clump} using the observed change in color during a “reddening” event (Equation 16):

$$\Delta A_V^{clump} = \frac{(z_g - z_r)_{obs} - (z_g - z_r)_0}{y_{z_g} - y_{z_r}}, \quad (46)$$

where $(z_g - z_r)_0$ is the “typical” value of $z_g - z_r$ for the apparent magnitude z_g . As shown in Figure 3, the most extreme reddening event occurred had:

$$(z_g - z_r)_{obs} \approx 2.25, \text{ and} \\ z_g \approx 20,$$

where, for this value of z_g , typically IC 10 X-2 has $(z_g - z_r)_0 \sim 1.25$. Therefore, during this event, $\Delta A_V^{clump} \sim 3$ – an increase larger than inferred to occur during the long duration flares (§4.1), and comparable to the average A_V^{tot} towards IC 10 X-2 inferred from previous X-ray observations (§4, Equation 12). This suggests the obscuring clump responsible this event had a Hydrogen column density $N_H^{clump} \sim 6 \times 10^{21} \text{ cm}^{-2}$ – comparable to what is inferred from hydrodynamic simulations to exist in such systems (e.g., El Mellah et al. 2018; Manousakis & Walter 2015a) and observations of similar systems (e.g., Grinberg et al. 2017).

Small scales “holes” in the distribution of material within this system (e.g., Manousakis & Walter 2015a; El Mellah et al. 2018) are unlikely to be responsible for epochs when IC 10 X-2 is “bluer” than average for a given magnitude since these structures are unlikely to

significantly decrease the total N_{H} along the line of sight (e.g., Grinberg et al. 2017). We therefore consider the possibility they are produced by a small, dense clump of material accreting onto the NS – as invoked to explain short-term increases in the X-ray flux from such sources (e.g., Manousakis & Walter 2015a) – whose resultant emission dominates over that from the SG companion over the duration of the accretion event. This is the same physical scenario discussed in §3.3 for the long duration flares, and during such events we expect emission in the observed bands to again be dominated by the Rayleigh-Jeans regime of the multi-temperature blackbody radiation generated by the accreting material, in which case the intrinsic colors of IC 10 X-2 will be those given in Equations 14 & 15. Assuming $A_{\text{V}}^{\text{tot}}$ (Equation 12) is the total extinction towards the NS during this events, the observed $(z_g - z_r)_{\text{blue}}$ color would be:

$$(z_g - z_r)_{\text{blue}} = (y_{z_g} - y_{z_r})A_{\text{V}}^{\text{tot}} + (z_g - z_r)_0 \quad (47)$$

$$\sim 0.43. \quad (48)$$

This value is comparable to the “bluest” emission observed from IC 10 X-2, $(z_g - z_r)_{\text{bluest}} \sim 0.5$ (Figure 3), suggesting that the decretion disk provides some additional absorption during this time. Since dense clumps are expected to be primarily near the decretion disk (e.g., Grinberg et al. 2017), additional absorption by the stellar wind material is not unexpected.

5. CONCLUSIONS

In this work, we performed a comprehensive analysis of a regular optical and near-infrared observations of IC 10 X-2 over a ~ 5 year period with the ZTF and LCO facilities, which measured the properties of this source in the g' / z_g , r' / z_r , and i' filters. Our analysis indicates IC 10 X-2 exhibits both periodic flaring and oscillations in its “quiescent” emission (§3.4), suggesting it is a BeHMXB, a Be star and neutron star orbiting each other with a ~ 26.5 day period – a designation consistent with previous identifications as a SFXT and sgHMXB (§4). When the NS enters the decretion disk generated by its stellar companion, the resultant accretion of material onto the NS generates the observed multi-day flares. During these flaring episodes, emission is expected to be dominated by the multi-temperature blackbody radiation emanating from material in the accretion disk around the NS. From the, nearly constant, color observed during these flares (§3.3), we infer that the column density towards IC 10 X-2 is $N_{\text{H}}^{\text{flare}} \sim 10^{22} \text{ cm}^{-2}$ (§4.1). This is $\sim 1.5 - 2 \times$ larger than the $N_{\text{H}}^{\text{tot}} \sim 6 \times 10^{21} \text{ cm}^{-2}$ inferred from the X-ray spectrum of this source (e.g., Laycock et al. 2014; §4) – the difference likely due to material in the

decretion disk along the line of sight. For the observed periodic (§3.4) changes in color and brightness (§3.2) of the “quiescent” emission of this source, we consider two possibilities (§4.2): orbital modulations in the column density along the line of sight (§4.2.1) or the varying contribution from a transient accretion disk around the NS (§4.2.2). We find that both explanations can reproduce our results: the first requires that, during the orbit, the N_{H} changes by $\Delta N_{\text{H}}^{\text{orb}} \sim 5.5 \times 10^{21} \text{ cm}^{-2}$ – comparable to the increase in N_{H} observed during the long duration flares (§4.2.1), while the second requires an accretion rate $\dot{M} \gtrsim 8 \times 10^{-10} M_{\odot} \text{ yr}^{-1}$ – larger than expected for the typical mass-loss rate of a Be star (§4.2.2). Lastly, during the campaign we also identified multiple epochs where the observed emission from IC 10 X-2 was significantly redder and bluer than typically observed for its apparent magnitude (§3.2 & §3.3). Since these episodes were typically confined to one epoch, their short durations ($\lesssim 1$ day) argue for existence of small scale structures, i.e. clumps, in material surrounding this binary system. Epochs where IC 10 X-2 is significantly “redder” than expected is likely to be the result of such clumps passing along the line of sight, with the largest observed change in color suggesting the clump had a column density $N_{\text{H}}^{\text{clump}} \sim 6 \times 10^{21} \text{ cm}^{-2}$ (§4.3). Epochs where IC 10 X-2 is significantly “bluer” than expected are possibly due to clumps accreting onto the NS, with the resultant emission dominating radiation in this band – a conclusion supported by the similarity of the bluest color observed by IC 10 X-2 and that expected from blackbody radiation after accounting for the interstellar N_{H} along this line (§4.3).

Many of these conclusions can be tested by similar monitoring of the UV and X-ray emission of this source, since increased accretion onto the NS should lead to increase in emission in these wavebands. If that is correct, we expect that the X-ray flux of IC 10 X-2 would increase, and possibly harden due to the increase N_{H} , during the observed optical flares. Furthermore, if a transient accretion disk is responsible for the observed periodic variations in the quiescent emission, a similar periodicity may also be observed in the X-ray band. Further monitoring in the bands discussed in this work (Table 1) would not only result in more examples of the transient behaviors described in this work, but could also lead to the discovery of longer timescale super-orbital variations (e.g., Kretschmar et al. 2019) – providing additional information regarding the interaction between the NS and its stellar companion in this HMXB.

ACKNOWLEDGMENTS

JA was supported by the Kawader Research Program at NYU Abu Dhabi, which is funded by the Executive Affairs Authority of the Emirate of Abu Dhabi through the administration of Tamkeen. Both JA and JDG received support from the NYU Abu Dhabi Research Institute grant to the CASS. COH is supported by NSERC Discovery Grant RGPIN-2016-04602. This research has made use of the SVO Filter Profile Service "Carlos Rodrigo", funded by MCIN/AEI/10.13039/501100011033/ through grant PID2020-112949GB-I00. This work has made use of the HMXB catalogue (<https://binary-revolution.github.io/HMXBwebcat/>) maintained by the Binary rEvolution team (<https://github.com/Binary-rEvolution>).

REFERENCES

- Alcock, C., Allsman, R. A., Alves, D. R., et al. 2001, *Monthly Notices of the Royal Astronomical Society*, 321, 678, doi: [10.1046/j.1365-8711.2001.04041.x](https://doi.org/10.1046/j.1365-8711.2001.04041.x)
- Bandyopadhyay, R. M., Wachter, S., Gelino, D., & Gelino, C. R. 2008, *A Population Explosion: The Nature & Evolution of X-ray Binaries in Diverse Environments*, 1010
- Bellm, E. C., Kulkarni, S. R., Graham, M. J., et al. 2019, *PASP*, 131, 018002, doi: [10.1088/1538-3873/aaecbe](https://doi.org/10.1088/1538-3873/aaecbe)
- Bird, T. 2012, *PoS, Extremesky 2011*, 012, doi: [10.22323/1.147.0012](https://doi.org/10.22323/1.147.0012)
- Bohlin, R. C., Savage, B. D., & Drake, J. F. 1978, *ApJ*, 224, 132, doi: [10.1086/156357](https://doi.org/10.1086/156357)
- Bozzo, E., Bernardini, F., Ferrigno, C., et al. 2017, *Astronomy & Astrophysics*, 608, A128, doi: [10.1051/0004-6361/201730398](https://doi.org/10.1051/0004-6361/201730398)
- Brown, T. M., Baliber, N., Bianco, F. B., et al. 2013, *Publications of the Astronomical Society of the Pacific*, 125, 1031, doi: [10.1086/673168](https://doi.org/10.1086/673168)
- Chaty, S. 2018, in *The Fourteenth Marcel Grossmann Meeting On Recent Developments in Theoretical and Experimental General Relativity, Astrophysics, and Relativistic Field Theories: Proceedings of the MG14 Meeting on General Relativity*, University of Rome "La Sapienza", Italy, 12–18 July 2015, World Scientific, 1883–1888
- Clark, J. S., Bartlett, E. S., Coe, M. J., et al. 2013, *Astronomy & Astrophysics*, 560, A10, doi: [10.1051/0004-6361/201321216](https://doi.org/10.1051/0004-6361/201321216)
- Coe, M. J., Kennea, J. A., Evans, P. A., et al. 2021, *Monthly Notices of the Royal Astronomical Society*, 504, 1398–1406, doi: [10.1093/mnras/stab972](https://doi.org/10.1093/mnras/stab972)
- Dickey, J. M., & Lockman, F. J. 1990, *ARA&A*, 28, 215, doi: [10.1146/annurev.aa.28.090190.001243](https://doi.org/10.1146/annurev.aa.28.090190.001243)
- Drave, S. P., Bird, A. J., Sidoli, L., et al. 2013, *MNRAS*, 433, 528, doi: [10.1093/mnras/stt754](https://doi.org/10.1093/mnras/stt754)
- Ducci, L., Sidoli, L., Mereghetti, S., Paizis, A., & Romano, P. 2009, *Monthly Notices of the Royal Astronomical Society*, 398, 2152–2165, doi: [10.1111/j.1365-2966.2009.15265.x](https://doi.org/10.1111/j.1365-2966.2009.15265.x)
- Ducci, L., Sidoli, L., & Paizis, A. 2010, *MNRAS*, 408, 1540, doi: [10.1111/j.1365-2966.2010.17216.x](https://doi.org/10.1111/j.1365-2966.2010.17216.x)
- Ducci, L., Mereghetti, S., Santangelo, A., et al. 2022, *A&A*, 661, A22, doi: [10.1051/0004-6361/202140867](https://doi.org/10.1051/0004-6361/202140867)
- El Mellah, I., Sundqvist, J. O., & Keppens, R. 2018, *MNRAS*, 475, 3240, doi: [10.1093/mnras/stx3211](https://doi.org/10.1093/mnras/stx3211)
- Foight, D. R., Güver, T., Özel, F., & Slane, P. O. 2016, *ApJ*, 826, 66, doi: [10.3847/0004-637X/826/1/66](https://doi.org/10.3847/0004-637X/826/1/66)
- Fortin, F., García, F., Simaz Bunzel, A., & Chaty, S. 2023, *A&A*, 671, A149, doi: [10.1051/0004-6361/202245236](https://doi.org/10.1051/0004-6361/202245236)
- Frank, J., King, A., & Raine, D. 2002, *Accretion Power in Astrophysics*, 3rd edn. (Cambridge University Press), doi: [10.1017/CBO9781139164245](https://doi.org/10.1017/CBO9781139164245)
- Gaia Collaboration, Vallenari, A., Brown, A. G. A., et al. 2023, *A&A*, 674, A1, doi: [10.1051/0004-6361/202243940](https://doi.org/10.1051/0004-6361/202243940)
- Gaudin, T. M., Kennea, J. A., Coe, M. J., et al. 2024, *Discovery of a Rare Eclipsing Be/X-ray Binary System*, Swift J010902.6-723710 = SXP 182. <https://arxiv.org/abs/2403.05648>
- González-Riestra, R., Oosterbroek, T., Kuulkers, E., Orr, A., & Parmar, A. N. 2004, *A&A*, 420, 589, doi: [10.1051/0004-6361:20035940](https://doi.org/10.1051/0004-6361:20035940)

- Goodwin, A. J., Russell, D. M., Galloway, D. K., et al. 2020, *Monthly Notices of the Royal Astronomical Society*, 498, 3429, doi: [10.1093/mnras/staa2588](https://doi.org/10.1093/mnras/staa2588)
- Gregory, P. C. 2002, *ApJ*, 575, 427, doi: [10.1086/341257](https://doi.org/10.1086/341257)
- Grinberg, V., Hell, N., El Mellah, I., et al. 2017, *A&A*, 608, A143, doi: [10.1051/0004-6361/201731843](https://doi.org/10.1051/0004-6361/201731843)
- Hainich, R., Oskinova, L. M., Torrejón, J. M., et al. 2020, *A&A*, 634, A49, doi: [10.1051/0004-6361/201935498](https://doi.org/10.1051/0004-6361/201935498)
- Hare, J., Halpern, J. P., Clavel, M., et al. 2019, *The Astrophysical Journal*, 878, 15, doi: [10.3847/1538-4357/ab1cbe](https://doi.org/10.3847/1538-4357/ab1cbe)
- HI4PI Collaboration, Ben Bekhti, N., Flöer, L., et al. 2016, *A&A*, 594, A116, doi: [10.1051/0004-6361/201629178](https://doi.org/10.1051/0004-6361/201629178)
- Jain, C., Paul, B., & Dutta, A. 2009, *Research in Astronomy and Astrophysics*, 9, 1303, doi: [10.1088/1674-4527/9/12/002](https://doi.org/10.1088/1674-4527/9/12/002)
- Kalberla, P. M. W., Burton, W. B., Hartmann, D., et al. 2005, *A&A*, 440, 775, doi: [10.1051/0004-6361:20041864](https://doi.org/10.1051/0004-6361:20041864)
- Karino, S., Nakamura, K., & Taani, A. 2019, *Publications of the Astronomical Society of Japan*, 71, doi: [10.1093/pasj/psz034](https://doi.org/10.1093/pasj/psz034)
- Kim, M., Kim, E., Hwang, N., et al. 2009, *ApJ*, 703, 816, doi: [10.1088/0004-637X/703/1/816](https://doi.org/10.1088/0004-637X/703/1/816)
- Kretschmar, P., Fürst, F., Sidoli, L., et al. 2019, *NewAR*, 86, 101546, doi: [10.1016/j.newar.2020.101546](https://doi.org/10.1016/j.newar.2020.101546)
- Kudritzki, R.-P., & Puls, J. 2000, *ARA&A*, 38, 613, doi: [10.1146/annurev.astro.38.1.613](https://doi.org/10.1146/annurev.astro.38.1.613)
- Kwan, S., Lau, R. M., Jencson, J., et al. 2018, *The Astrophysical Journal*, 856, 38, doi: [10.3847/1538-4357/aaaf73](https://doi.org/10.3847/1538-4357/aaaf73)
- Lamers, H. J. G. L. M., & Cassinelli, J. P. 1999, *Introduction to Stellar Winds*
- Lamers, H. J. G. L. M., Zickgraf, F.-J., de Winter, D., Houziaux, L., & Zorec, J. 1998, *A&A*, 340, 117
- Lau, R. M., Tinyanont, S., Hankins, M. J., et al. 2021, *The Astrophysical Journal*, 922, 5, doi: [10.3847/1538-4357/ac2237](https://doi.org/10.3847/1538-4357/ac2237)
- Laycock, S., Cappallo, R., Oram, K., & Balchunas, A. 2014, *The Astrophysical Journal*, 789, 64, doi: [10.1088/0004-637x/789/1/64](https://doi.org/10.1088/0004-637x/789/1/64)
- Liu, Q. Z., Chaty, S., & Yan, J. Z. 2011, *MNRAS*, 415, 3349, doi: [10.1111/j.1365-2966.2011.18949.x](https://doi.org/10.1111/j.1365-2966.2011.18949.x)
- Lomb, N. R. 1976, *Ap&SS*, 39, 447, doi: [10.1007/BF00648343](https://doi.org/10.1007/BF00648343)
- Manousakis, A., & Walter, R. 2011, *A&A*, 526, A62, doi: [10.1051/0004-6361/201015707](https://doi.org/10.1051/0004-6361/201015707)
- . 2015a, *A&A*, 575, A58, doi: [10.1051/0004-6361/201321414](https://doi.org/10.1051/0004-6361/201321414)
- . 2015b, *A&A*, 584, A25, doi: [10.1051/0004-6361/201526893](https://doi.org/10.1051/0004-6361/201526893)
- Martínez-Núñez, S., Kretschmar, P., Bozzo, E., et al. 2017, *SSRv*, 212, 59, doi: [10.1007/s11214-017-0340-1](https://doi.org/10.1007/s11214-017-0340-1)
- Mauron, N., & Josselin, E. 2011, *A&A*, 526, A156, doi: [10.1051/0004-6361/201013993](https://doi.org/10.1051/0004-6361/201013993)
- Monageng, I. M., Coe, M. J., Kennea, J. A., et al. 2019, *MNRAS*, 489, 993, doi: [10.1093/mnras/stz2262](https://doi.org/10.1093/mnras/stz2262)
- Monageng, I. M., Coe, M. J., Buckley, D. A. H., et al. 2020, *MNRAS*, 496, 3615, doi: [10.1093/mnras/staa1739](https://doi.org/10.1093/mnras/staa1739)
- NASA. 2021, *NASA/IPAC Infrared Science Archive (IRSA)*, NASA. <https://science.nasa.gov/astrophysics/astrophysics-data-centers/nasa-ipac-infrared-science-archive>
- Oskinova, L. M., Hamann, W.-R., & Feldmeier, A. 2007, *Astronomy & Astrophysics*, 476, 1331–1340, doi: [10.1051/0004-6361:20066377](https://doi.org/10.1051/0004-6361:20066377)
- Pellizza, L. J., Chaty, S., & Negueruela, I. 2006, *A&A*, 455, 653, doi: [10.1051/0004-6361:20054436](https://doi.org/10.1051/0004-6361:20054436)
- Rampy, R. A., Smith, D. M., & Negueruela, I. 2009, *ApJ*, 707, 243, doi: [10.1088/0004-637X/707/1/243](https://doi.org/10.1088/0004-637X/707/1/243)
- Rodrigo, C., & Solano, E. 2020, in *XIV.0 Scientific Meeting (virtual) of the Spanish Astronomical Society*, 182
- Rodrigo, C., Solano, E., & Bayo, A. 2012, *SVO Filter Profile Service Version 1.0, IVOA Working Draft 15 October 2012*, doi: [10.5479/ADS/bib/2012ivoa.rept.1015R](https://doi.org/10.5479/ADS/bib/2012ivoa.rept.1015R)
- Russell, D. M., Maitra, D., Fender, R. P., & Lewis, F. 2008, *Unifying disc-jet behaviour in X-ray binaries: an optical/IR approach*. <https://arxiv.org/abs/0811.2919>
- Russell, D. M., Bramich, D. M., Lewis, F., et al. 2019, *Astronomische Nachrichten*, 340, 278–283, doi: [10.1002/asna.201913610](https://doi.org/10.1002/asna.201913610)
- Scargle, J. D. 1982, *ApJ*, 263, 835, doi: [10.1086/160554](https://doi.org/10.1086/160554)
- Schmidtke, P. C., Cowley, A. P., & Udalski, A. 2021, *Research Notes of the American Astronomical Society*, 5, 130, doi: [10.3847/2515-5172/ac0640](https://doi.org/10.3847/2515-5172/ac0640)
- Shakura, N., Postnov, K., Sidoli, L., & Paizis, A. 2014, *Monthly Notices of the Royal Astronomical Society*, 442, 2325, doi: [10.1093/mnras/stu1027](https://doi.org/10.1093/mnras/stu1027)
- Shakura, N. I., Postnov, K. A., Kochetkova, A. Y., et al. 2015, *Astronomy Reports*, 59, 645, doi: [10.1134/s1063772915070112](https://doi.org/10.1134/s1063772915070112)
- Shakura, N. I., & Sunyaev, R. A. 1973, *A&A*, 24, 337
- Shi, C.-S., Zhang, S.-N., & Li, X.-D. 2015, *The Astrophysical Journal*, 813, 91, doi: [10.1088/0004-637x/813/2/91](https://doi.org/10.1088/0004-637x/813/2/91)
- Sidoli, L. 2013, *Supergiant Fast X-ray Transients: a review*, arXiv, doi: [10.48550/ARXIV.1301.7574](https://doi.org/10.48550/ARXIV.1301.7574)
- Tan, C. 2021, *Journal of Physics: Conference Series*, 2012, 012119, doi: [10.1088/1742-6596/2012/1/012119](https://doi.org/10.1088/1742-6596/2012/1/012119)

- Townsend, L. J., Coe, M. J., Corbet, R. H. D., & Hill, A. B. 2011, *Monthly Notices of the Royal Astronomical Society*, 416, 1556, doi: [10.1111/j.1365-2966.2011.19153.x](https://doi.org/10.1111/j.1365-2966.2011.19153.x)
- Treiber, H., Vasilopoulos, G., Baily, C. D., et al. 2021, *MNRAS*, 503, 6187, doi: [10.1093/mnras/stab807](https://doi.org/10.1093/mnras/stab807)
- VanderPlas, J. T. 2018, *The Astrophysical Journal Supplement Series*, 236, 16, doi: [10.3847/1538-4365/aab766](https://doi.org/10.3847/1538-4365/aab766)
- Walter, R., Zurita-Heras, J., & Leyder, J. C. 2007, Probing clumpy stellar winds with a neutron-star. <https://arxiv.org/abs/0712.1931>
- Wang, Q. D., Whitaker, K. E., & Williams, R. 2005, *MNRAS*, 362, 1065, doi: [10.1111/j.1365-2966.2005.09379.x](https://doi.org/10.1111/j.1365-2966.2005.09379.x)
- Wegner, W. 2006, *MNRAS*, 371, 185, doi: [10.1111/j.1365-2966.2006.10549.x](https://doi.org/10.1111/j.1365-2966.2006.10549.x)
- Whittet, D. C. B. 2022, *Dust in the Galactic Environment (Third Edition)*, doi: [10.1088/2514-3433/ac7204](https://doi.org/10.1088/2514-3433/ac7204)
- Yuan, H. B., Liu, X. W., & Xiang, M. S. 2013, *Monthly Notices of the Royal Astronomical Society*, 430, 2188, doi: [10.1093/mnras/stt039](https://doi.org/10.1093/mnras/stt039)
- Zhu, H., Tian, W., Li, A., & Zhang, M. 2017, *Monthly Notices of the Royal Astronomical Society*, 471, 3494, doi: [10.1093/mnras/stx1580](https://doi.org/10.1093/mnras/stx1580)
- ZTF. 2022, *Public Data Releases, DR6, ZTF*, doi: [10.5281/zenodo.15991](https://doi.org/10.5281/zenodo.15991)